# An automatic change detection method for monitoring newly constructed building areas using time-series multi-view high-resolution optical satellite images

Xin Huang[a,b,*,1], Yinxia Cao[a,1], Jiayi Li[a]

[a] School of Remote Sensing and Information Engineering, Wuhan University, Wuhan 430079, PR China
[b] State Key Laboratory of Information Engineering in Surveying, Mapping and Remote Sensing, Wuhan University, Wuhan 430079, PR China

## ARTICLE INFO

## ABSTRACT

Automatically monitoring newly constructed building areas (NCBAs) is essential for efficient land resource management and sustainable urban development, particularly in the rapidly urbanizing country of China. In this regard, time-series multi-view high-resolution optical satellite images can provide fine spatial details for clearly characterizing NCBAs, but this leads to great heterogeneity and complexity, owing to the high spectral variation, complicated imaging conditions, and different viewing angles. Moreover, to date, the vertical features and time-series information from these images have not been fully exploited for urban change detection. In this paper, our primary objective is to automatically detect the presence of NCBAs, and meanwhile, to investigate the feasibility of identifying their change timing using time-series multi-view ZY-3 high-resolution satellite images. To this aim, we propose an automatic change detection method consisting of three components: 1) firstly, we jointly use planar-vertical features to delineate the NCBAs; 2) object-based temporal correction is subsequently applied to improve the spatiotemporal consistency of the features; and 3) finally, a multi-temporal change detection model is used to simultaneously capture the NCBAs and the change timing. We applied the method on two urban fringe areas of Beijing (7 multi-temporal image sets) and Shanghai (7 multi-temporal image sets), respectively, which are cities that have been experiencing rapid urbanization. The experimental results confirmed the effectiveness of the proposed method. For both study areas, the F-score values reached nearly 90% in terms of NCBA detection, and with respect to the change timing, the overall accuracies with a one-year tolerance strategy reached around 92%. The joint use of the planar-vertical features and the inclusion of multi-temporal images make the proposed method a promising approach for automatically providing the spatiotemporal information of NCBAs in practical applications.

## 1. Introduction

Extensive urbanization is commonly accompanied by physical expansion of urban land, especially in Asia and Africa (Bren d'Amour et al., 2017). For instance, in the rapidly urbanizing Asian country of China, a great deal of non-urban land (e.g., arable land, pastures, forests, lakes) is being converted into newly constructed building areas (NCBAs) (Y. Li et al., 2015; J. Liu et al., 2014; Y. Liu et al., 2014; Liu et al., 2018; J. Wang et al., 2012; Zhou et al., 2017). The newly constructed building areas (NCBAs) refer to the areas that are dominated by new buildings, ancillary roads and greenbelts, and they are usually constructed for residential, commercial, industrial zones, and public facilities, according to the China's land-use classification scheme (SAC,

2017). Although these newly constructed regions can relieve the population pressure and promote economic development, they have threatened the quality of arable land (Kong, 2014) and induced severe environmental degradation (Bai et al., 2016; Liu et al., 2018).

In this context, the government of China has started to strictly confine NCBAs to specific areas by implementing the three "red line" policies, which are the ecological conservation redline (ECR) (Bai et al., 2016), the prime farmland protection boundary (PFPB) (Xia et al., 2016), and the urban growth boundary (UGB) (Jian et al., 2017). Nevertheless, some illegal cases of land occupation are still taking place (ChinaDaily, 2015), destroying the areas that are under the protection of the three red line policies project. Moreover, the prevalence of NCBAs poses a great threat to food security (Bren d'Amour et al., 2017),

---

freshwater availability (Cohen, 2011), climate change (Fu and Weng, 2016; Sun et al., 2016), and forest ecosystem services and biodiversity (He et al., 2017, 2014; Potapov et al., 2012). Therefore, monitoring NCBAs has become the focus of the China's Ministry of Natural Resources (ChinaDaily, 2017), and it is imperative to characterize the spatiotemporal dynamics of NCBAs, in order to enhance land resource management and guarantee sustainable urban development.

Remotely sensed imagery, with the notable advantages of the various spectral, spatial, and temporal resolutions, as well as the wide coverage, is increasingly utilized to investigate urban land expansion (Ban et al., 2017; Ban and Yousif, 2012; Del Frate et al., 2008; Gamba et al., 2006; Grey et al., 2003; Lefebvre et al., 2016; Mertes et al., 2015; Taubenböck et al., 2019, 2012; L. Wang et al., 2012; Zhou et al., 2018). Recently, the availability of high-resolution (with a spatial resolution of < 5 m) satellite data, e.g., IKONOS, QuickBird, WorldView-1/2/3, Pléiades-1A/1B, ZY-3 01/02, GF-1/2, TerraSAR-X, and COSMO-SkyMed, is opening up new avenues for dynamic urban monitoring at a very fine scale (Bouziani et al., 2010; Leichtle et al., 2017; Marin et al., 2015; Mendez Dominguez et al., 2019; Pacifici et al., 2007; Zhang et al., 2017). Specifically, the detailed spatial information provided by the high-resolution images makes it possible to mitigate the mixed pixel problem existing in the moderate-to-coarse images, and can therefore characterize NCBAs more clearly. Nevertheless, to date, identifying NCBAs has been totally reliant on visual interpretation (ChinaDaily, 2019), in practice, leading to a high cost in terms of time and effort, especially when conducted in large areas. Therefore, for the considerations of practical use, it is well worth developing automatic change detection methods without manual sampling, in order to derive NCBAs from the huge amount of high-resolution data.

However, most initiatives to automatically monitor urban land expansion using high-resolution optical satellite images are hampered by: a) the limited data availability caused by the low temporal resolution and cloud contamination; and b) the heterogeneity and complexity (i.e., the high spectral variation, complicated imaging conditions, and different viewing angles) (Bruzzone and Bovolo, 2013; Chen et al., 2012). These factors pose great challenges to the traditional change detection methods (Tewkesbury et al., 2015). Generally speaking, change detection can be conducted at bi-temporal (i.e., identifying the differences of two images at a time) or multi-temporal (i.e., time-series analysis with multiple images) timescales (Coppin et al., 2004). While bi-temporal methods have been widely adopted (Ban and Yousif, 2012; Bovolo and Bruzzone, 2007; Gamba et al., 2006; Ridd and Liu, 1998; Teo and Shih, 2013; Xian et al., 2009), multi-temporal methods have shown great potential for providing a more in-depth understanding of land-cover dynamics in recent years (Zhu, 2017). For instance, many researchers have proposed multi-temporal or time-series change detection algorithms for moderate-to-coarse resolution images, such as LandTrendr (Kennedy et al., 2010), the vegetation change tracker (VCT) (Huang et al., 2010), the breaks for additive season and trend (BFAST) algorithm (Verbesselt et al., 2010), and continuous change detection and classification (CCDC) (Zhu and Woodcock, 2014). However, most of these algorithms have been developed for vegetative ecosystems, which may experience multidirectional changes (e.g., forestry disturbance or recovery), and thus they are not suitable for monitoring urban land expansion, since this is typically unidirectional (i.e., the inverse change is unrealistic) (Schneider, 2012). In this regard, Song et al. (2016) adopted a logical function to model the impervious surface cover change, and then extracted the change magnitude, timing, and duration over a 27-year span (Sexton et al., 2013). More recently, Li et al. (2018) developed a temporal segmentation method based on linear regression, and identified the urban land conversion sources (i.e., vegetation, water, and bare soil) during 1985–2015. These methods can characterize the urban land expansion process as three continuous stages (pre-change, change, and post-change), based on sufficient time-series images.

Synthetic aperture radar (SAR) images have received much attention on urban change detection, as they are not affected by weather conditions (Ban and Yousif, 2012; Del Frate et al., 2008; Gamba et al., 2007, 2006; Hu and Ban, 2014; Mendez Dominguez et al., 2019; Su et al., 2015; Yang et al., 2017). For example, Gamba et al. (2006) extracted linear features from bi-temporal SAR images to detect changed pixels. By using time-series SAR images, Su et al. (2015) combined a likelihood ratio test and a clustering-and-recognizing method to identify different change types in urban areas. Furthermore, Mendez Dominguez et al. (2019) utilized the backscatter and height differences from high-resolution tomographic SAR image pairs to perform 2D and 3D urban change detection. However, most of these methods are specific to SAR images which are prone to intrinsic speckle noise (Hu and Ban, 2014), and thus they can be not directly applied to optical images. In this research, the multi-view high-resolution (< 5 m) optical satellite images are focused on. To the knowledge of the authors, the existing urban change detection studies seldom take into account time series of high-resolution (< 5 m) optical satellite images, owing to the difficulties in data acquisition and image processing, as well as the lack of specific application scenarios. Recently, Sentnel-2 data, with a spatial resolution of 10 *m* and a revisit time of 5 days at the equator (Drusch et al., 2012), has been employed to urban change detection (Ban et al., 2017; Benedetti et al., 2018; Haas and Ban, 2018; Lefebvre et al., 2016). However, single buildings and small settlements may be omitted due to the limitation of the spatial resolution of Sentinel-2 data (Pesaresi et al., 2016). Therefore, high-resolution (< 5 m) optical images are essential to find and analyze the micro-scale changes (e.g., NCBAs) and the timing of the changes.

Some progress has been made on high-resolution image change detection. For instance, the inclusion of spatial/contextual information (e.g., texture, structure, and spatial relationships) has often been considered to complement the spectral features and suppress false alarms (Bruzzone and Bovolo, 2013). Examples are the gray-level co-occurrence matrix (GLCM) (Lefebvre and Corpetti, 2017), wavelet decomposition (Celik and Ma, 2011), morphological profiles (MPs) (Falco et al., 2013; Mura et al., 2008), and edge features (Rowe and Grewe, 2001). Furthermore, object-based change detection (OBCD), which focuses on image objects instead of individual pixels, is more effective for analyzing multi-temporal high-resolution images, due to its superiorities in both facilitating the multiscale modeling of spatial information and mitigating the "salt-and-pepper" effect induced by registration errors, spectral variability, and imaging conditions (Chen et al., 2012; Hussain et al., 2013). Consequently, a wide range of studies have applied spatial information derived from image objects or the context of pixels (e.g., a local neighborhood) to improve the performance of change detection. For example, Im et al. (2008) developed an object-based correlation image analysis approach, under the assumption that the correlation significantly decreased from unchanged objects to changed objects; Bovolo (2009) introduced a multilevel parcel-based technique to model multi-temporal images, and subsequently employed multilevel change vector analysis (CVA) to produce change maps; Pacifici and Del Frate (2010) compared the signal values of pulse-coupled neural networks (PCNNs) between bi-temporal images to derive changed areas; Tang et al. (2011) proposed an object-based Kolmogorov-Smirnov test to detect the changes between pairs of image objects by judging whether their probability distributions were similar under a predefined significance level; Wen et al. (2016) measured the patch-based (i.e., a fixed-size window) histogram similarity of multiple indices (i.e., the morphological building index, enhanced vegetation index, and normalized difference water index) to recognize the difference of the spatial arrangements between bi-temporal images; and Xiao et al. (2016) employed a series of morphological operators to transform the analysis unit from pixels to objects, and made full use of the spectral and textural features to detect changed objects.

In contrast to planar features (e.g., spectrum, texture, and structure), vertical features can provide three-dimensional (3D) information for describing off-terrain objects (e.g., buildings) (Li et al., 2020), and

thus they have been widely applied to urban change detection (Qin et al., 2016), such as radar (e.g., scatterometer, interferometric, and tomographic synthetic aperture radar) (Balk et al., 2019; Montazeri et al., 2016; Weissgerber et al., 2017), Light Detection and Ranging (LiDAR) (Teo and Shih, 2013), and Digital Surface Models (DSM) from stereo-/multi-view optical imageries (Chaabouni-Chouayakh and Reinartz, 2011; Guerin et al., 2014). Particularly, in the domain of high-resolution urban change detection, vertical features have been increasingly studied (Che et al., 2018; Leichtle et al., 2017; Mendez Dominguez et al., 2019; Qin, 2014; Stal et al., 2013; Tian et al., 2014; Yang et al., 2017). For instance, Stal et al. (2013) calculated the difference of DSMs derived from stereoscopic aerial images on date 1 and LiDAR on date 2 to generate the 3D building change result. Tian et al. (2014) measured the difference of DSMs on two dates through the Kullback–Leibler (KL) divergence similarity (Inglacla and Mercier, 2007) to produce building change maps. Leichtle et al. (2017) proposed an unsupervised object-based clustering method to detect changed buildings by using bi-temporal high resolution satellite images and DSM. Che et al. (2018) performed 2D and 3D urban change detection by applying a multivariate Gaussian mixed model to bi-temporal Quad-PolSAR images at the superpixel level. However, it should be noted that, owing to shadowing and layover effects, radar data cannot provide precise shapes of ground objects (e.g., buildings) (Gamba and Houshmand, 2000). By contrast, LiDAR can deal with this issue but they usually have a limited coverage due to the high cost. In this regard, high resolution stereo optical images hold great potentials for retrieving 3D information with fine shape details at a low cost. However, to the knowledge of the authors, time-series and multi-view high-resolution optical satellite images have not been investigated for urban change detection. In summary, the aforementioned work has been devoted to dealing with the relevant challenges, but the following key issues in high-resolution image change detection have not been investigated:

1) The vertical features can provide three-dimensional information when describing complex urban scenes, and thus deserve comprehensive investigation. Nevertheless, in the current literature, vertical features from multi-view high-resolution optical satellite imageries, as well as their joint use with planar features, have seldom been considered for urban change detection.

2) A large number of the existing methods addressing high-resolution change detection are not based on the nadir-view images, due to the difficulty in acquiring time-series high-resolution images with the nadir view or the same view angle. However, the nadir view is the premise of an accurate and fair comparison between multi-temporal images, and can also reduce the spurious changes caused by angular differences.

3) Most of the existing high-resolution change detection methods have been designed for use with bi-temporal images, while multi-temporal images have rarely been considered. In this context, the time-series information has not been fully exploited for the change detection. Moreover, the previous studies have usually failed to identify the timing of the changes, owing to the lack of time-series information.

In this context, it has now become possible to address the aforementioned research limitations, courtesy of the Chinese ZY-3 high-resolution stereo satellite constellation. The constellation consists of ZY-3 01 and its successor ZY-3 02, launched in January 2012 and May 2016, respectively. Each satellite can simultaneously acquire three panchromatic images with ± 22° forward/backward (3.5 m spatial resolution for ZY-3 01 and 2.5 m for ZY-3 02) and nadir (2.1 m) viewing angles, and one multispectral (5.8 m) image (Huang et al., 2017). The four images constitute an image set, where the multi-view images can provide effective representations of the vertical features, and the multispectral image can be used to extract abundant spectral, textural, and structural features. In addition, the nadir-view cameras carried on the

ZY-3 satellites can be expected to substantially reduce the spurious changes induced by the different viewing angles between multi-temporal high-resolution images (Huang et al., 2017).

In this paper, our primary objective is to automatically detect the presence of NCBAs, and meanwhile, to investigate the feasibility of identifying their change timing from time-series multi-view ZY-3 images. The change timing refers to the start point of building construction. To achieve this goal, we propose an automatic change detection method consisting of three components: 1) firstly, we jointly use the planar-vertical features to describe the NCBAs; 2) subsequently, we apply object-based temporal correction to improve the spatiotemporal consistency of the features; and 3) finally, a multi-temporal change detection model based on the second-order difference (SOD) is used to capture the NCBAs and the timing of the changes.

The rest of this paper is organized as follows. Section 2 introduces the study areas and data, which is followed by a detailed description of the proposed method in Section 3. The experimental results are presented in Section 4. The performance of the method is then discussed in Section 5. Finally, Section 6 concludes the paper.

## 2. Study areas and data

The two Chinese megacities of Beijing and Shanghai were selected to test the proposed method, since they have been experiencing rapid urban land expansion in recent decades (Fei and Zhao, 2019). Land transformation, such as the presence of NCBAs, often occurs in urban-rural fringes where land resources (e.g., cultivated land, forest land, barren land) are adequate for the construction of new building areas (X. Li et al., 2015). Therefore, in this research, we focused on the urban fringe areas of the two cities (Fig. 1a–b).

Beijing, the capital of China, situated in the north of the North China Plain, has long been a prosperous and populous metropolis. Its permanent population amounted to 21.71 million in 2017 (NBSC, 2018). The study site, as shown in Fig. 1a, covers an area of approximately 689.23 km$^2$ and encompasses an urban-suburban-rural transition from north to south. This study area presents a mixture of arable land and building areas, and is thus well suited for testing the proposed method.

Shanghai, the largest megacity in China (UN, 2018), located in the south of the Yangtze River Delta, had a permanent population of 24.18 million in 2017 (NBSC, 2018). Fig. 1b displays the study area covering an area of about 413.25 km$^2$. Compared to Beijing, this area shows a distinct pattern, in terms of geographic location and direction of urban expansion (from west to east), and thus it is suitable to further verify the generalization ability of the proposed method.

All available ZY-3 01/02 images between 2012 and 2018 and with cloud cover of < 10% were collected (Fig. 1c–d and Table 1). There were a total of 14 multi-temporal image sets from ZY-3 01 (12 sets) and ZY-3 02 (two sets) for Beijing, and a total of eight multi-temporal image sets from ZY-3 01 (six sets) and ZY-3 02 (two sets) for Shanghai. Please note that each ZY-3 image set contains four images acquired simultaneously in the same area, i.e., three panchromatic images (forward, backward, and nadir viewing angles) and one multispectral image with four bands (blue, green, red, and near-infrared). Considering the sparse temporal distribution of ZY-3 data in two study areas, we used one image for each year at similar acquisition time. The effect of inconsistent temporal information on monitoring NCBAs is analyzed in Section 5.3.

## 3. Methodology

The proposed change detection method for monitoring the spatiotemporal dynamics of NCBAs consists of three components: 1) planar-vertical feature extraction for delineating NCBAs; 2) object-based temporal correction for improving the spatiotemporal consistency of the features; and 3) multi-temporal change detection for capturing the NCBAs and their change timing (Fig. 2). Details of each component are
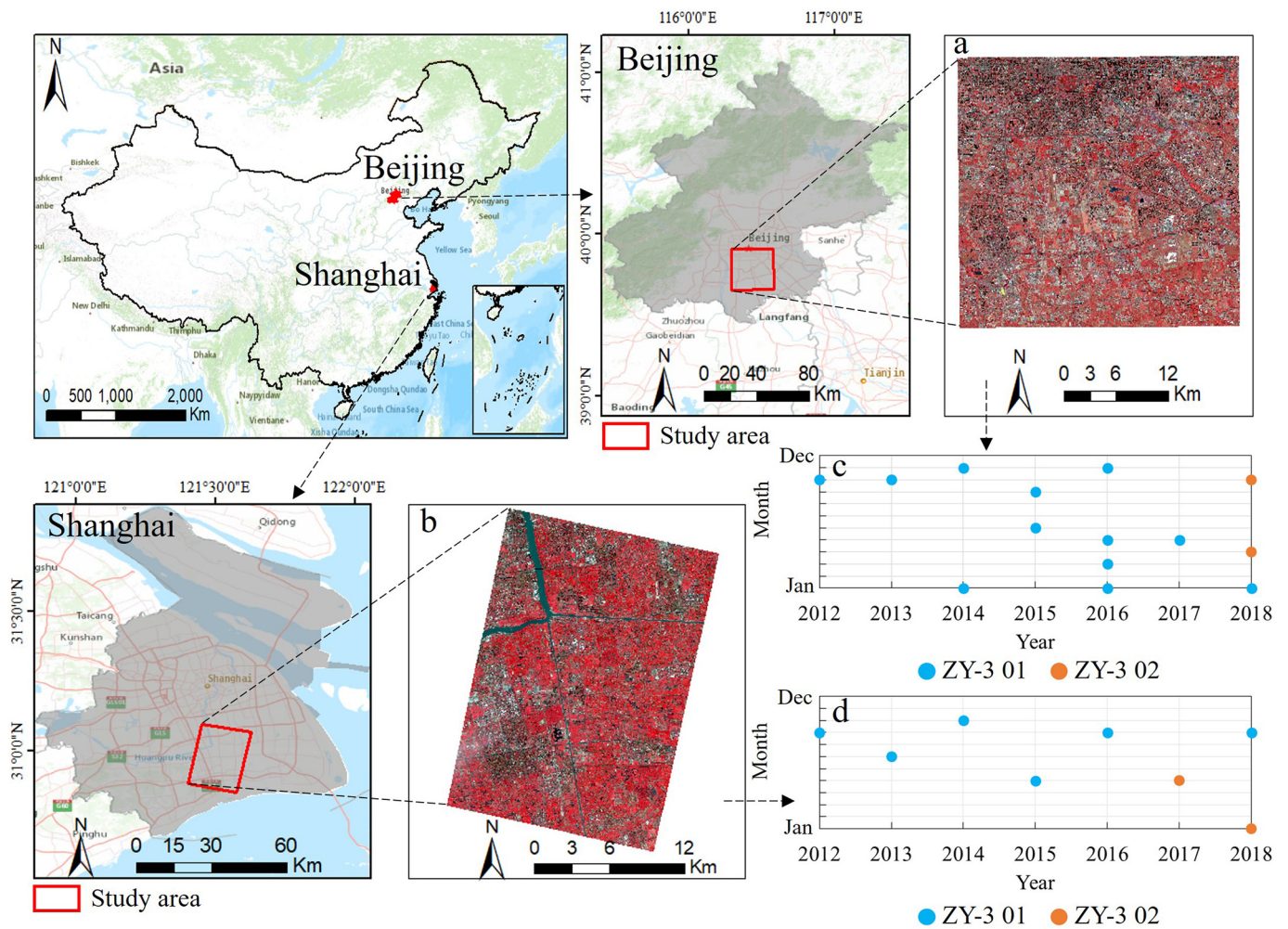
**Fig. 1.** The two study areas and the temporal distribution of the ZY-3 images. (a) and (b) False-color images (R: near-infrared, G: red, B: green), acquired on Oct. 6, 2018, and Sept. 30, 2018, respectively. (c) and (d) The temporal distribution of the ZY-3 01/02 images for Beijing and Shanghai, respectively. The spatial extents of the study areas a and b are 689.23 km² and 413.25 km², respectively. (For interpretation of the references to color in this figure legend, the reader is referred to the web version of this article.)

presented below.

### 3.1. Pre-processing

Multi-temporal ZY-3 image sets were preprocessed in four steps: 1) digital surface model (DSM) generation; 2) image-to-image registration; 3) orthorectification and pan-sharpening; and 4) radiometric correction. The details of each steps are described as follows.

Firstly, the nadir-forward stereo pair was employed to generate DSM, since this stereo pair usually performs better than nadir-backward

and forward-backward pairs (Liu et al., 2017), and the DSM was subsequently used for extracting normalized DSM (nDSM), i.e., the relative height of off-terrain objects above the ground (see Section 3.2). The key steps for DSM generation involved: 1) the nadir-forward stereo pair was rectified to a quasi epipolar stereo pair (Wang et al., 2011), based on the rational polynomial coefficients (RPCs) provided by the China Centre for Resources Satellite Data and Application (CRESDA); 2) the hierarchical semi-global matching (SGM) algorithm (Hirschmüller, 2008) was performed on the epipolar images to generate the disparity map; and 3) the three-dimensional (3D) point clouds were obtained by

**Table 1**

The available ZY-3 multi-temporal images (cloud cover < 10%) of Beijing and Shanghai. Images marked with "*" are ZY-3 02 images, while the others are ZY-3 01. Date "2012-10-11" corresponds to "year-month-day".

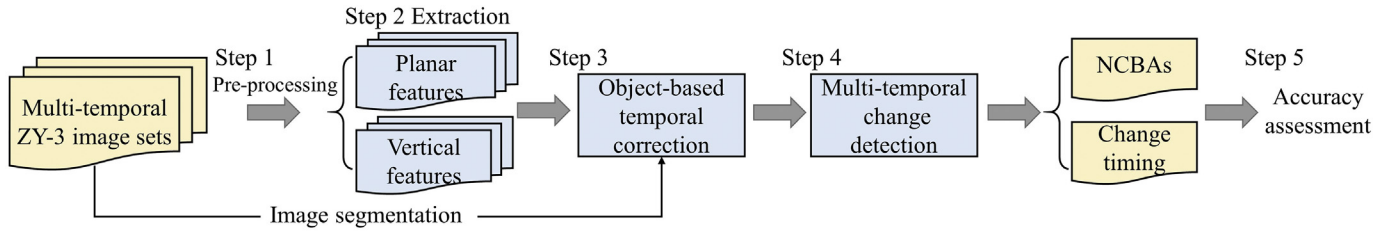| City | Acquisition date | | | | | | | Angle number | Study area |
|---|---|---|---|---|---|---|---|---|---|
| | 2012 | 2013 | 2014 | 2015 | 2016 | 2017 | 2018 | | (km²) |
| Beijing | 10–11 | 10–10 | 01–21 | 06–02 | 01–24 | 05–15 | 01–01 | 3 | 689.23 |
| | | | 11–17 | 09–23 | 03–23 | | 04–07* | 3 | |
| | | | | | 05–21 | | 10–06* | 3 | |
| | | | | | 11–24 | | | 3 | |
| Shanghai | 09–18 | 07–10 | 10–15 | 05–05 | 09–03 | 05–14* | 01–15* | 3 | 413.25 |
| | | | | | | | 09–30 | 3 | |

**Fig. 2.** The workflow of the proposed change detection method. NCBAs: newly constructed building areas.

forward intersection, and then were resampled into a raster grid, followed by inverse distance interpolation for filling the holes caused by matching failures (Qin, 2014). The root mean square error (RMSE) of DSM derived from ZY-3 satellite images is about 3.9–6.9 m in the urban area (Fratarcangeli et al., 2016), and the RMSE of nDSM derived from DSM is about 10 m in terms of building height estimation (Liu et al., 2017). Note that low or repetitive textures and occlusions of buildings can sometimes degrade the performance of DSM (Hirschmüller, 2008), leading to underestimation of the low-rise buildings (e.g., site 2 in Fig. 8). Therefore, in the proposed method, we jointly used planar-vertical feature fusion to alleviate the uncertainty of DSM.

Secondly, all off-nadir (i.e., forward/backward-view) and multispectral images were geometrically registered to the same nadir-view image by polynomial warping using the automatically identified tie points (Kennedy and Cohen, 2003), with a registration error of < 1 pixel, and all the images were then resampled to 2.5 m. In this study, the forward/backward/nadir-view images were registered, so that we can utilize the angular difference between them to obtain the vertical information of buildings for monitoring NCBAs (see Section 3.2).

Thirdly, the multispectral and nadir images were orthorectified with the generated DSM, and subsequently were fused by the Gram-Schmidt algorithm (Laben and Brower, 2000) to improve the spatial resolution of multispectral images.

Finally, in order to reduce the radiometric differences between the multi-view image series, the pseudo-invariant features method (Schott et al., 1988) was applied to the time series of multispectral images and nadir images, and the off-nadir images were normalized to the nadir images of the same date by the histogram matching method (Gonzalez and Woods, 2002).

### 3.2. Planar-vertical feature extraction

A total of three planar features and three vertical features were used for delineating the different properties of NCBAs (Table 2). The nadir panchromatic images were used as the base images to extract the MBI, MSI, Harris, and PanTex features. Detailed descriptions of these features are presented as follows.

#### 3.2.1. Planar features

(a) The morphological building index (MBI)

The MBI (Huang and Zhang, 2011) depicts the structural properties

**Table 2**
The planar and vertical features used to delineate NCBAs. Base images include the nadir (NAD), forward (FWD), and backward (BWD) panchromatic images.

| Type | Feature | Property | Base image |
|------|---------|----------|------------|
| Planar | MBI | Structure | NAD |
| | Harris | Corner | NAD |
| | PanTex | Texture | NAD |
| Vertical | MSI | Shadow | NAD |
| | nDSM | Height | NAD and FWD |
| | MABI | Angle | NAD, FWD and BWD |

of buildings with multiscale and multidirectional morphological operators, based on the fact that buildings usually exhibit a higher brightness than their surroundings and display distinct structural characteristics (i.e., size, directionality, and shape). It is defined as:

$$\text{MBI} = \frac{\sum_{s,d} \text{DMP}_{\text{WTH}}(s, d)}{N_s \times N_d} \tag{1}$$

with

$$\text{WTH}(s, d) = \text{NAD} - \gamma_{\text{NAD}}(s, d) \tag{2}$$

where $\text{DMP}_{\text{WTH}}$ denotes the differential morphological profiles (DMPs) of the white top-hat by reconstruction (WTH); $N_s$ and $N_d$ refer to the total number of scale $s$ and directionality $d$, respectively; and $\gamma_{\text{NAD}}$ is the opening-by-reconstruction of the nadir panchromatic image (NAD) with multiple linear structural elements. Note that the structural element is determined by $s$ and $d$. In this study, we set $s$ in the range of [2, 150] with an interval of 37 ($N_s = 4$), according to the spatial resolution of the images (2.5 m) and the size of the buildings in the study areas. Four directions ($N_d = 4$) were considered: 0°, 45°, 90°, and 135°.

(b) The Harris corner detector (Harris)

The Harris corner detector (Harris and Stephens, 1988) is used to detect the corners of buildings by measuring the image intensity changes caused by all possible shifts of a predefined window. The Harris corner response is expressed as a function of determinant *det* and trace *tr* of the symmetric matrix M:

$$\text{Harris} = det(M) - k \cdot tr^2(M) \tag{3}$$

with

$$M = \sum_{x=1}^{N_w} \sum_{y=1}^{N_w} w(x, y) \begin{bmatrix} I_x^2 & I_x I_y \\ I_x I_y & I_y^2 \end{bmatrix} \tag{4}$$

where $I_x$ and $I_y$ denote the image derivatives in the horizontal and vertical directions, respectively; and $w(x, y)$ defines the weight of pixel $(x, y)$ within a window. A Gaussian window with the size of 12.5 m and a standard deviation of 2 was selected due to the low sensitivity to noise (Harris and Stephens, 1988), and the trade-off scalar $k$ was empirically set to 0.04.

(c) The texture-derived built-up presence index (PanTex)

The PanTex index (Pesaresi et al., 2008) represents the textural characteristics of building areas, and is defined as the minimum value of multiple contrast metrics (CON), each of which is derived from a gray-level co-occurrence matrix (GLCM):

$$\text{CON} = \sum_{i=0}^{N_g-1} \sum_{j=0}^{N_g-1} (i - j)^2 P(i, j) \tag{5}$$

where $P(i, j)$ signifies the $(i, j)$th entry of the GLCM (determined by a window and a displacement vector), and $N_g$ is the number of image gray levels. The window size and gray levels were set to 50 *m* and 256, respectively, and 10 combinations of displacement vectors were selected

according to Pesaresi et al. (2008).

### 3.2.2. Vertical features

(a) The morphological shadow index (MSI)

The MSI (Huang and Zhang, 2012) highlights building shadows, which can indicate the height and location of buildings (Liasis and Stavrou, 2016). The basic idea of the MSI is that shadows often show lower brightness and similar structure features when compared with their spatially adjacent buildings:

$$\text{MSI} = \frac{\sum_{s,d} \text{DMP}_{\text{BTH}}(s, d)}{N_s \times N_d} \tag{6}$$

with

$$\text{BTH}(s, d) = \varphi_{\text{NAD}}(s, d) - \text{NAD} \tag{7}$$

where $\text{DMP}_{\text{BTH}}$ denotes the DMP of black top-hat by reconstruction (BTH), and $\varphi_{\text{NAD}}$ specifies the closing-by-reconstruction of the nadir panchromatic image (NAD). Scale $s$, directionality $d$, and the number of $s$ and $d$ ($N_s$ and $N_d$, respectively) were set the same as those of the MBI, in terms of the high correlation between shadows and buildings.

(b) The normalized digital surface model (nDSM)

The nDSM (Qin and Fang, 2014) indicates the relative height of buildings above the ground, and is generally obtained by subtracting the height of the terrain from the digital surface model (DSM). Courtesy of the nadir-forward stereo pairs acquired by the ZY-3 satellites (Liu et al., 2017), we generated the DSM by the widely used semi-global matching (SGM) algorithm (Hirschmüller, 2008), and then performed top-hat reconstruction on the DSM to remove the height of the terrain:

$$\text{nDSM} = \text{DSM} - \rho_{\text{DSM}}(\varepsilon) \tag{8}$$

where $\rho_{\text{DSM}}(\varepsilon)$ indicates the morphological reconstruction of the mask image (DSM) from the marker image. Specifically, the marker image was generated by eroding the mask image with a disk-shaped structural element. The radius of the structural element was set to 75 m, according to the size of the largest buildings in the study areas (Qin and Fang, 2014).

(c) The multi-angular built-up index (MABI)

The MABI (Liu et al., 2019) depicts the angular properties of buildings, based on the inconsistent response of buildings (i.e., spectral and structural variations) to different viewing angles. In this study, we applied the normalized difference MABI to quantify the angular differences of buildings:

$$\text{MABI} = \max\left\{ \frac{|I_n - I_f|}{\max(I_n, I_f)}, \frac{|I_n - I_b|}{\max(I_n, I_b)}, \frac{|I_f - I_b|}{\max(I_f, I_b)} \right\} \tag{9}$$

where $I_n$, $I_f$, and $I_b$ correspond to the spectral values of the nadir, forward, and backward panchromatic images, respectively. A large MABI value indicates a large angular difference between multi-view images, and hints at the presence of buildings.

Fig. 3 shows two examples of planar-vertical features located in residential (a) and industrial (b) areas, respectively. The structures with high feature values are more likely to be building areas. It can be seen that these complex and diverse building areas are effectively distinguished from non-building areas (e.g., main roads and bare land) by these features. For instance, the dark building areas (sites 1 and 2) are highlighted by the vertical descriptors, i.e., MSI, nDSM, and MABI, while the low-rise bright building areas (site 3) are indicated by the textural properties, i.e., MBI, Harris, and PanTex.

### 3.3. Object-based temporal correction

We implemented object-based temporal correction for improving the spatiotemporal consistency of the features through the following two steps.

Step 1. Object-based segmentation. Firstly, a linear 2% stretch was applied to normalize each feature into [0, 1]. The widely used multi-resolution segmentation algorithm (Baatz and Schäpe, 2000) was then employed to partition the last one of the time-series images into objects. Finally, for each object, the value of each feature was assigned as the mean value over all the internal pixels. It should be stressed that the selection of an optimal segmentation scale is challenging, but in this study, a small scale (i.e., 50) was set, considering that over-segmentation is preferable to under-segmentation, since the latter often leads to an undesired mixture of buildings and their surroundings (Huang and Zhang, 2012). The effect of scale is further analyzed in Section 5.2.

Step 2. Temporal correction for removing abnormal fluctuations in the original time series of features, such as ephemeral "spikes" or "dips". Under the widely accepted assumption that the conversion from non-urban land to urban land is irreversible during a short time period (Schneider, 2012), the values of building features (i.e., the planar-vertical features in Table 2) do not generally decrease after construction. The rule can be written as:

$$\widehat{F}_{i,t} = \begin{cases} F_{i,t-1} \\ \quad if\ F_{i,t} < F_{i,t-1} \\ F_{i,t} \\ \quad otherwise \end{cases} \tag{10}$$

where $F_{i,t}$ and $F_{i,t-1}$ signify the original features for object i at time t and $t-1$ respectively; and $\widehat{F}_{i,t}$ is the corrected feature for object i at time t. Based on this rule, we corrected the original time series of each feature for each object. Note that t can start from the beginning (forward direction) or end (backward direction) of the time series, which may bias the features (Hu and Huang, 2019). In this study, we took the average of the two directions as the corrected feature. The effect of temporal correction is further discussed in Section 5.2.

### 3.4. Multi-temporal change detection

We carried out multi-temporal change detection to capture the NCBAs and their change timing. The basic idea is that NCBAs often exhibit a distinctive temporal pattern, which can be characterized by the time series of planar-vertical features. Fig. 4 illustrates typical time series of planar-vertical features for NCBAs and non-NCBAs. For the NCBAs, the values of the building features in the non-building areas are generally low at the beginning of the time series, and then rise either gradually or sharply during the period of construction, and eventually become stable after completion (Fig. 4a). In contrast, for the cases of non-NCBAs (Fig. 4b–f), the values of the building features mostly stay at a high or low level, and are relatively stable over the entire study period.

Based on the distinctive temporal pattern of NCBAs, we first calculated the dynamics of three consecutive feature values within a moving temporal window (the red rectangle in Fig. 5a). It is formulated as:

$$D_{i,t} = (F_{i,t+1} - F_{i,t}) - (F_{i,t} - F_{i,t-1}) \tag{11}$$

where $F_{i,t-1}$, $F_{i,t}$, and $F_{i,t+1}$ denote the values of the building feature $F$ for object $i$ at times $t-1$, $t$, and $t+1$, respectively. On the one hand, if the first term ($F_{i,t+1} - F_{i,t}$) is significantly greater than the second term ($F_{i,t} - F_{i,t-1}$), the pattern of the three feature values (i.e., $F_{i,t-1}$, $F_{i,t}$, and $F_{i,t}$
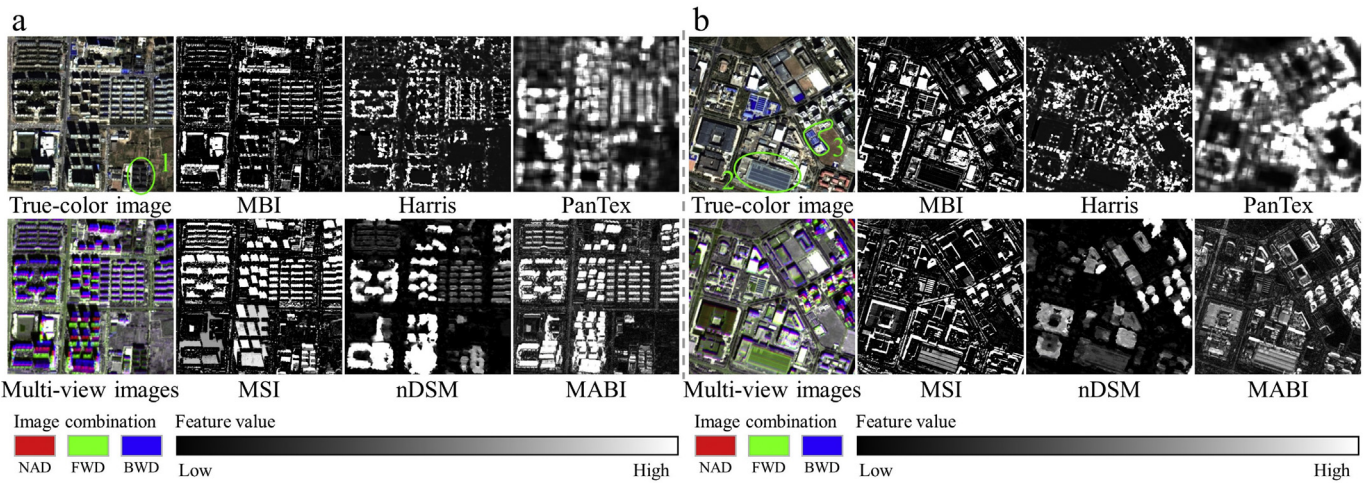
**Fig. 3.** Two examples of planar-vertical features in Beijing. (a) Residential areas (1 km by 1 km). (b) Industrial areas (1 km by 1 km). The multi-view images are displayed as the combination of the nadir (NAD), forward (FWD), and backward (BWD) panchromatic images.

$_{+1}$) is likely to be 'low-low-high', indicating that the feature value begins to increase significantly. The point with the maximum value of $D_{i, t}$ (the blue point in Fig. 5b) is regarded as the change start point $Q_1$ (the blue point in Fig. 5a). On the other hand, if the first term is significantly less than the second term, the pattern is close to 'low-high-high', signifying that the feature value starts to stabilize. The point with the minimum value of $D_{i, t}$ (the red point in Fig. 5b) is identified as the change end point $Q_2$ (the red point in Fig. 5a). Particularly, when there is little difference between the first and second term, the change of feature values is relatively stable. By searching for the stage between $Q_1$ and $Q_2$, we determined the point with the maximum increment of the feature value as the change point, corresponding to the change timing.

We then calculated the difference of the mean value between the stage after $Q_2$ and before $Q_1$ as the change magnitude of each feature (Fig. 5a). In this way, the time-series information was taken into account. A larger change magnitude indicates a higher probability of the presence of NCBAs. Furthermore, we applied a threshold to the change magnitude to extract NCBAs. The threshold was set as α times the standard deviation from the mean of the change magnitude (Xian et al., 2009). Accordingly, an object was classified as "NCBA", if its change magnitude exceeded the threshold, and as "non-NCBA" otherwise. In this study, α was set to 1.0, according to Morisette and Khorram (2000).

Finally, we fused the results of all the features (Table 2) to determine the final NCBAs and their change timings, since a single building feature is not reliable and is usually subject to omission and commission errors in terms of the spatiotemporal complexity and
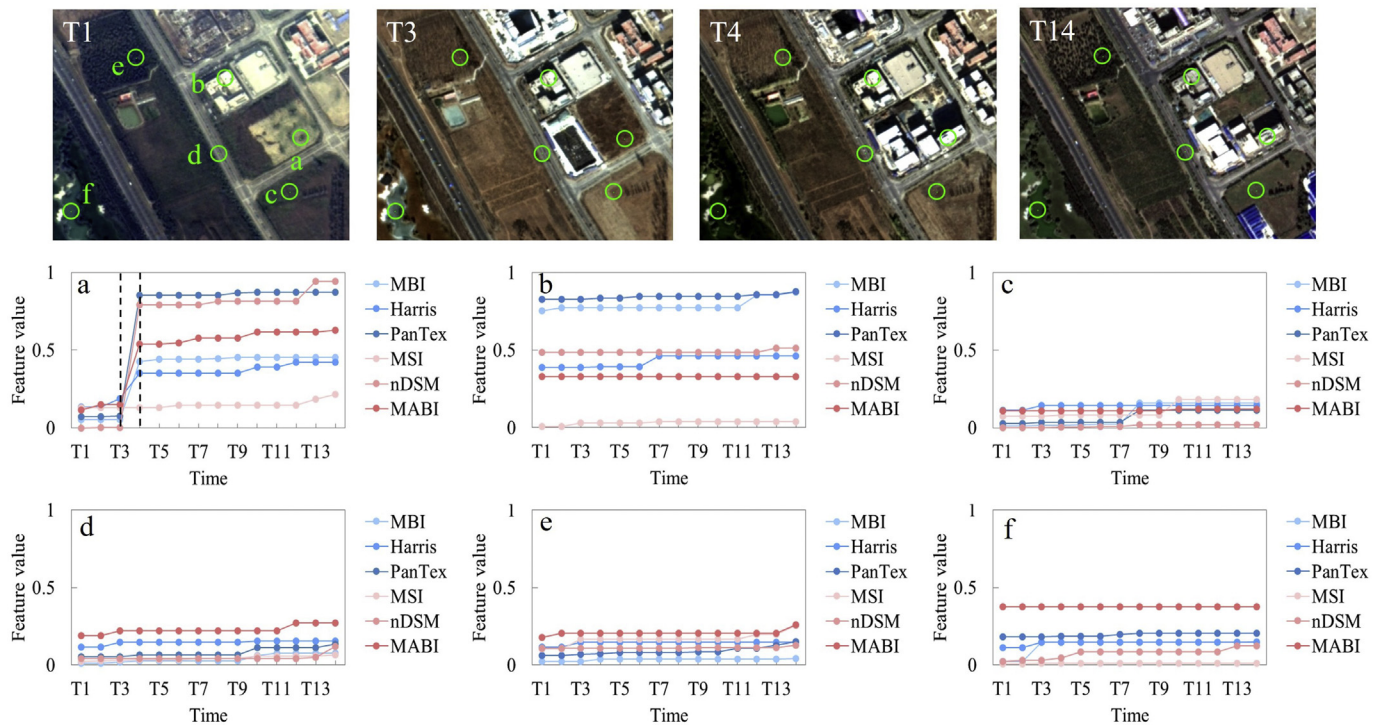


**Fig. 4.** Typical time series of planar-vertical features for NCBAs and non-NCBAs. The time Ti ($i = 1, 2, …$) corresponds to the acquisition date of the $i$ th image (see Table 1). The six graphs denote the time-series features in the center pixels of the green circles. The two dashed black lines in graph (a) indicate the change stage (i.e., T3–T4).The spatial extent of this region is 827.5 m by 700 m. (For interpretation of the references to color in this figure legend, the reader is referred to the web version of this article.)
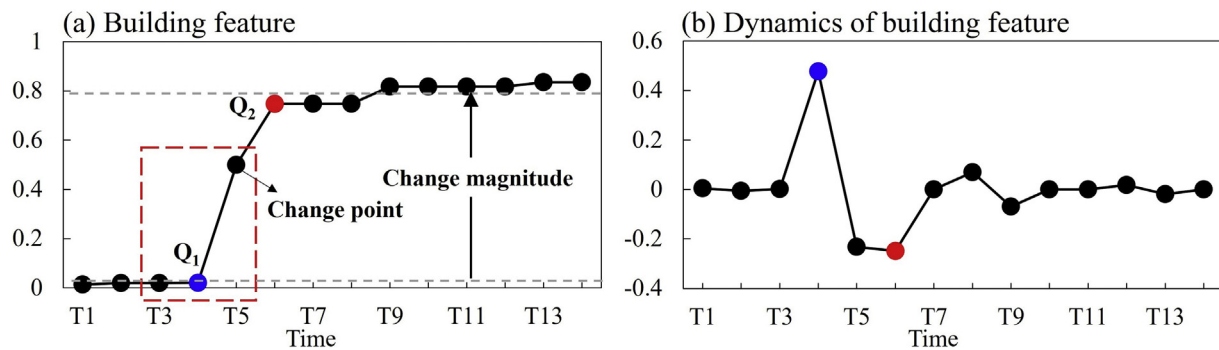
**Fig. 5.** The building feature curve (a) and the dynamics of feature value (b). $Q_1$: the change start point; $Q_2$: the change end point. The red rectangle denotes three consecutive feature values within a temporal window. The two dashed gray lines mark the mean feature values at the stages before $Q_1$ and after $Q_2$, respectively. For the first and last dates, we add the temporally nearest feature values to complete the three consecutive feature values. (For interpretation of the references to color in this figure legend, the reader is referred to the web version of this article.)

heterogeneity of ground objects. In detail, an object was identified as an NCBA if confirmed by at least two features, and we then performed weighted voting on the change timing of these features. Specifically, the weight was set to 1 for MBI, Harris, PanTex, and MSI, and 2 for nDSM and MABI, given that the latter two features are extracted from multi-view images and are therefore less affected by illumination variations (Qin et al., 2016).

### 3.5. Accuracy assessment

To evaluate the performance of the proposed method, we visually interpreted the NCBAs (dominated by new buildings) and non-NCBAs (i.e., persistent building areas or persistent non-building areas), and identified the change timings when the NCBAs appeared, assisted with the nadir multi-temporal ZY-3 images and very high resolution images from Google Earth. Please notice that if a NCBA only contains an isolated building (e.g., a large factory), it was delineated individually. In addition, the minimum mapping unit was set to 400 m², according to the requirement of the Ministry of Natural Resources of the People's Republic of China, implying that an NCBA with a size of < 400 m² would not be considered. Fig. 6a and c show the reference data collected in the two study areas.

In view of the small proportion of NCBAs, we adopted the stratified random sampling scheme with equal allocation (Olofsson et al., 2014; Stehman, 2012) to generate 1000 test samples (in pixels), where 500 samples were from NCBAs and 500 samples were from non-NCBAs, based on the reference data. A minimum distance of 100 m was set to reduce the spatial autocorrelation between test samples. We assessed the accuracy of the NCBA detection using the F-score metric (Powers, 2011), which is the harmonic mean of the user's accuracy (UA) and the producer's accuracy (PA). For those samples that were correctly detected as NCBAs by our method, we calculated their change timing accuracy using the overall accuracy (OA) metric. Specifically, considering that lots of building construction would take several years to complete, which may induce confusions between neighboring years for detecting change timing, we adopted two matching strategies. The first was the exact match, in that the detected change timing was considered as correct if it was consistent with the reference change timing, while the second strategy refers to a one-year tolerance, in that the detected change timing was considered as correct if it was in the range of ± 1 year of the reference change timing (Song et al., 2016). In order to achieve a high statistical confidence in the accuracy assessment, we created 10 independent test sets (i.e., 10 × 1000 samples), and we report the mean and standard deviation of each accuracy metric.

### 4. Results

Fig. 6 illustrates the identified NCBAs and their change timing

results in Beijing and Shanghai. In the two study areas, most of NCBAs are located in low-density urban areas with adequate land for building construction, involving individual large buildings (e.g., large factories) or a group of buildings (e.g., residential blocks). Our method can effectively detect these NCBAs, such as those dominated by compact buildings (sites 1, 3 and 8), large buildings (sites 2 and 4), detached high-rise buildings (site 5), and residential blocks (sites 7 and 9), by courtesy of their distinct texture, structure, and height attributes. In addition, a few of NCBAs are located in high-density urban areas, involving a single or several buildings owing to the limitation of land and space. In these areas, our approach can effectively detect large or high buildings, e.g., site 6 (Fig. 6), but may miss small and low buildings, due to the low response of planar-vertical features. Other irrelevant objects, e.g., newly constructed roads (in the top-left corner of region g), unchanged building areas, and rivers, are successfully suppressed by the proposed method, since the features we employ are focused on building areas from both planar and vertical viewpoints.

Table 3 presents the accuracies of the NCBAs for Beijing and Shanghai. In general, the proposed method shows a promising accuracy for NCBA detection, with the mean F-score value being 90.2% and 91.4% for Beijing and Shanghai, respectively. Table 4 and Table 5 reveal the accuracies of the change timings for Beijing and Shanghai, respectively. We can observe that the one-year tolerance strategy increases the mean OA from 68.9% to 93.0% for Beijing, and from 77.1% to 92.3% for Shanghai, compared to the exact match. The results quantitatively demonstrate that the proposed method can not only detect the NCBAs accurately, but it can also determine their change timings, based on the time-series multi-view ZY-3 images.

### 5. Discussion

#### 5.1. Performance of the planar-vertical features

To evaluate the performance of the planar-vertical features in detecting NCBAs and their change timings, we compared individual planar/vertical features (planar: MBI, Harris, PanTex; vertical: MSI, nDSM, MABI) and their combinations. All single and fused features have been aggregated into the object level. Fig. 7 shows the accuracies of the NCBAs and their change timings for the different feature combinations in both Beijing and Shanghai.

With regard to the NCBA detection (Fig. 7a and b), the planar-vertical joint features obtain the highest F-score values, and the producer's accuracies are significantly improved, in both study areas. It is shown that the 2D-3D fused features can greatly reduce the omission errors, while not increasing the false alarms. It is interesting to see that the MSI (shadow features) achieves a high UA but a very low PA, indicating that the shadow features can correctly detect NCBAs, but are subject to large omission errors. This property actually makes the MSI suitable for
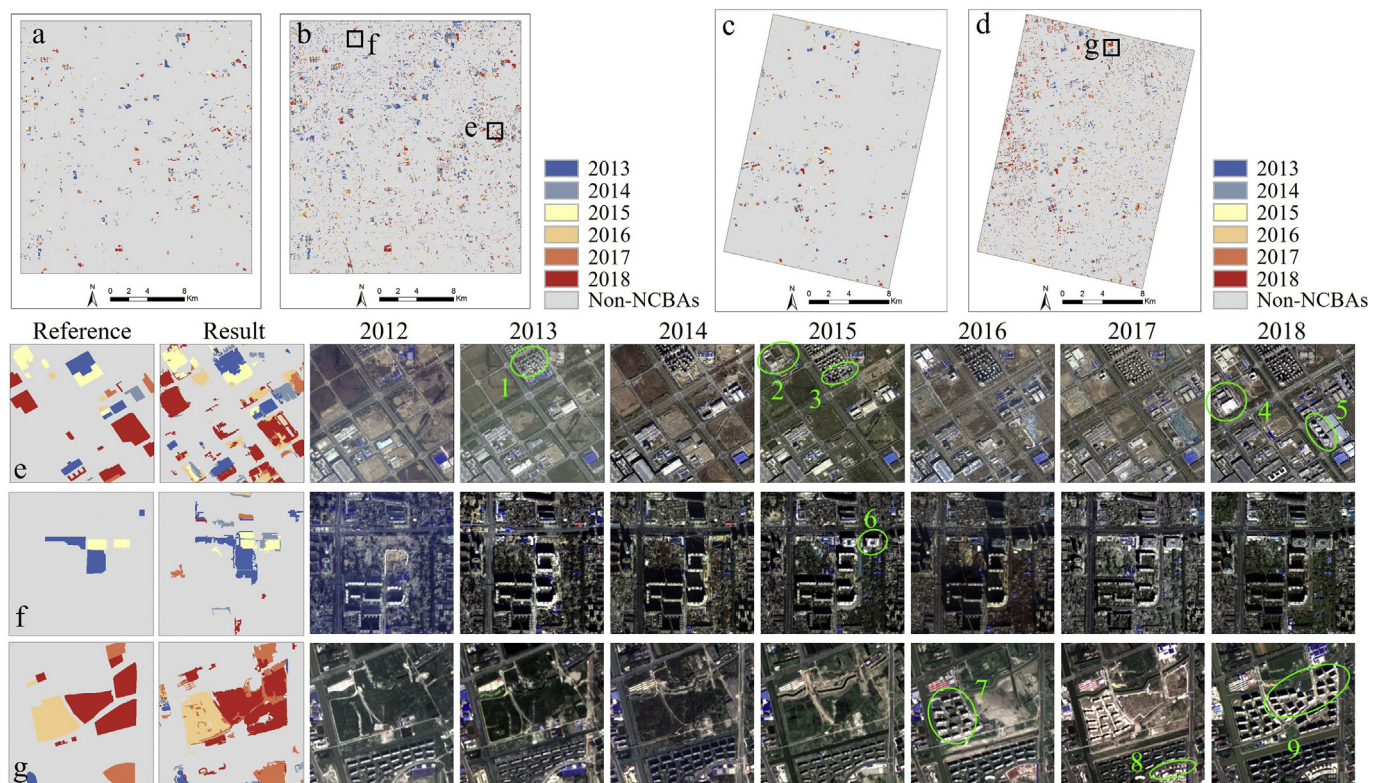
**Fig. 6.** The identified NCBAs and their change timing results. (a) and (c) The reference data for Beijing and Shanghai, respectively. (b) and (d) The NCBAs and change timing results detected by the proposed method for Beijing and Shanghai, respectively. The last three rows show the zoomed-in areas (black rectangles) of the reference data, detection result, and the multi-temporal ZY-3 images. The spatial extents of regions e, f, and g are 1.48 km by 1.52 km, 0.95 km by 0.89 km, and 1 km by 1 km, respectively.

**Table 3**
The accuracies (%) of the NCBAs for Beijing and Shanghai. UA: user's accuracy; PA: producer's accuracy.

|          | UA           | PA           | F-score      |
|----------|--------------|--------------|--------------|
| Beijing  | 92.5 ± 1.0   | 88.1 ± 1.1   | 90.2 ± 0.8   |
| Shanghai | 94.3 ± 1.1   | 88.7 ± 1.3   | 91.4 ± 0.9   |

**Table 4**
The accuracies (%) of the change timings with the exact match and the one-year tolerance strategies for Beijing. UA: user's accuracy; PA: producer's accuracy; OA: overall accuracy.

| Year | Exact match | | One-year tolerance | |
|------|------|------|------|------|
|      | UA           | PA           | UA           | PA           |
| 2013 | 74.3 ± 4.6   | 82.8 ± 3.4   | 93.5 ± 2.3   | 95.6 ± 1.2   |
| 2014 | 81.6 ± 2.5   | 73.9 ± 3.1   | 96.5 ± 1.3   | 95.2 ± 1.9   |
| 2015 | 55.4 ± 5.2   | 62.3 ± 7.0   | 88.8 ± 5.4   | 87.6 ± 5.4   |
| 2016 | 35.6 ± 3.9   | 70.1 ± 6.5   | 86.9 ± 5.2   | 86.7 ± 4.4   |
| 2017 | 71.5 ± 7.4   | 30.6 ± 3.7   | 95.7 ± 2.0   | 92.1 ± 3.5   |
| 2018 | 78.1 ± 3.7   | 86.0 ± 3.8   | 89.0 ± 4.4   | 92.7 ± 2.7   |
|      | OA           | 68.9 ± 2.0   | OA           | 93.0 ± 1.5   |

**Table 5**
The accuracies (%) of the change timings with the exact match and the one-year tolerance strategies for Shanghai. UA: user's accuracy; PA: producer's accuracy; OA: overall accuracy.

| Year | Exact match | | One-year tolerance | |
|------|------|------|------|------|
|      | UA           | PA           | UA           | PA           |
| 2013 | 77.4 ± 4.2   | 83.1 ± 4.1   | 93.8 ± 3.3   | 93.1 ± 3.0   |
| 2014 | 82.5 ± 2.2   | 78.8 ± 4.6   | 95.4 ± 1.2   | 92.4 ± 1.9   |
| 2015 | 65.2 ± 7.1   | 50.5 ± 7.8   | 89.8 ± 3.9   | 87.3 ± 4.7   |
| 2016 | 84.4 ± 3.8   | 78.9 ± 3.4   | 94.6 ± 2.0   | 91.5 ± 2.0   |
| 2017 | 56.2 ± 5.5   | 73.2 ± 6.8   | 93.5 ± 3.0   | 96.9 ± 2.7   |
| 2018 | 78.9 ± 3.8   | 81.6 ± 4.1   | 85.8 ± 4.1   | 92.7 ± 1.6   |
|      | OA           | 77.1 ± 1.3   | OA           | 92.3 ± 0.9   |

fusion with other features, since it is able to strengthen the completeness of the results, without triggering commission errors.

In terms of the change timings with the two matching strategies (Fig. 7c and d), we can observe that nDSM and MABI perform better than the other single features, verifying the superiority of the multiview features in identifying the change timings of the NCBAs. For the feature fusion, the planar-vertical fusion achieves comparable results to the planar or vertical feature fusion in the case of change timing, but

the former outperforms the latter in detecting NCBAs. Overall, the joint use of planar-vertical features is able to make use of the different features, and yields satisfactory results.

Fig. 8 illustrates an example of the NCBAs and their change timing results for the different feature combinations. All single and fused features have been aggregated into the object level. Different from the pixel-level features (e.g., spectral features), the six features employed in this study are actually defined in a spatial context to represent building areas. The MBI and MSI were constructed on a series of linear neighborhood (i.e., structural elements), although they were calculated on a per-pixel basis (Huang and Zhang, 2012). Considering that MBI and MSI can indicate the presence of buildings and their spatially adjacent shadows, respectively, they actually describe the spatial context of the NCBAs. The Harris employed the possible shifts of a predefined window to measure the image intensity changes for identifying the corners of buildings (Harris and Stephens, 1988). The PanTex used a local window to extract textural features, which can characterize built-ups as well as
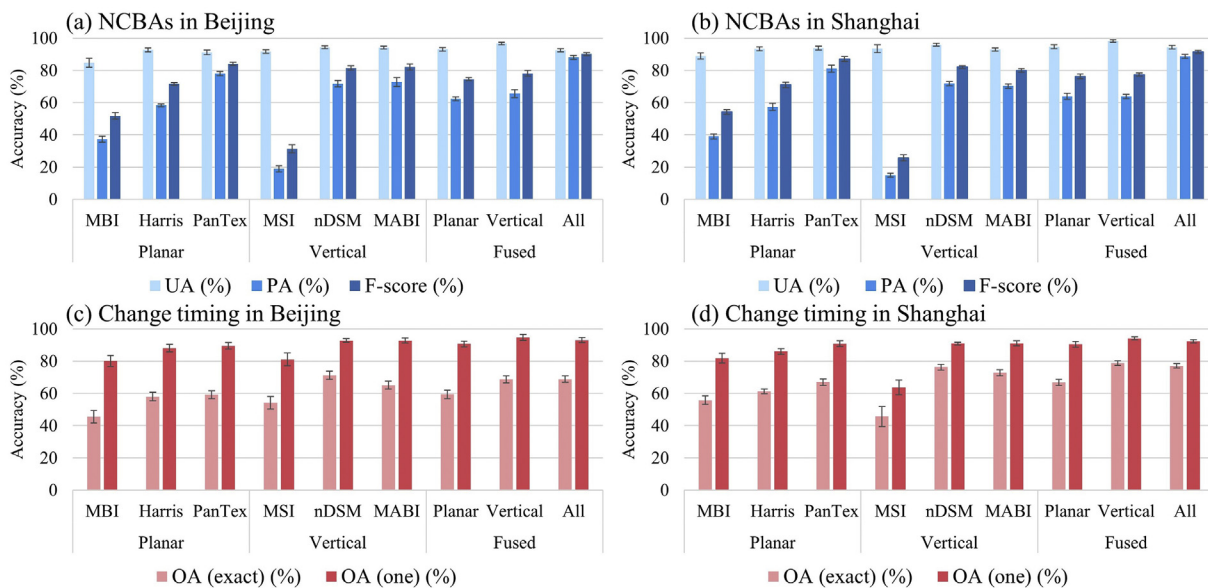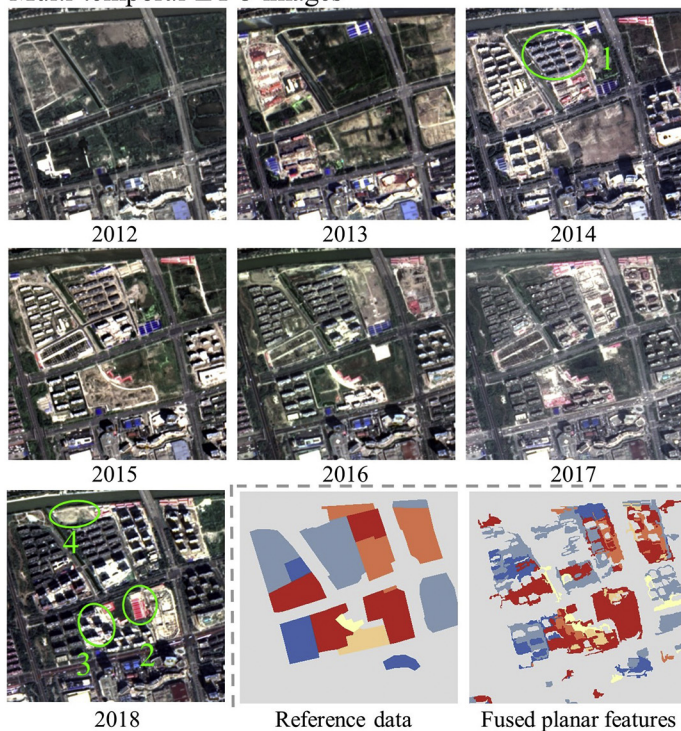
Fig. 7. The accuracies of the NCBAs and their change timings for the different feature combinations in both Beijing and Shanghai. All: planar-vertical features; UA: user's accuracy; PA: producer's accuracy; OA: overall accuracy; exact: exact match; one: one-year tolerance.
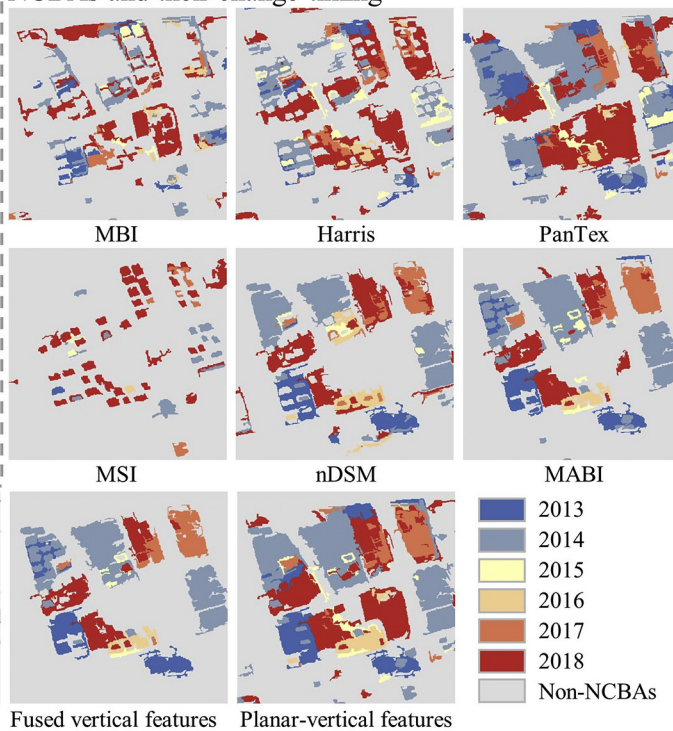


Fig. 8. An example (1 km by 1 km) of the NCBAs and their change timing results for the different feature combinations in Shanghai.

their neighborhoods (Pesaresi et al., 2008). The nDSM utilized the height difference between buildings and the terrain within a local neighborhood to obtain the relative height of buildings above the ground (Qin and Fang, 2014). The MABI employed the different responses of buildings to different viewing angles in a local context to extract the vertical properties of buildings (Liu et al., 2019).

In site 1, it can be seen that PanTex, nDSM, and MABI successfully detect the dark NCBAs, due to their efficacy in describing the textural and vertical properties. In site 2, the low-rise bright NCBAs are effectively identified by the planar features, i.e., MBI, Harris, and PanTex. In this case, it is found that the planar features are more sensitive to the

low-rise building areas with high brightness and conspicuous textures, compared to the vertical features. In site 3, nDSM and MABI successfully capture the change timings, and the MSI effectively identifies the shadows adjacent to newly constructed buildings. In site 4, our approach can suppress the noise of the flat bare land, which is falsely detected by MBI but is filtered out by the fusion of planar-vertical features. In summary, we can observe that the single features and fused planar/vertical features are subject to missed or false detections owing to the diversity and complexity of building areas, but their joint use can capture more complete NCBAs and accurate change timings.

In addition, we also collected samples at the pixel level and further

**Table 6**

The accuracies (%) of NCBAs and change timing with both pixel-level and object-level assessment in Beijing and Shanghai. UA: user's accuracy; PA: producer's accuracy; OA: overall accuracy; exact: exact match; one: one-year tolerance.

| | | NCBAs | | | Change timing | |
|---|---|---|---|---|---|---|
| | | UA | PA | F-score | OA (exact) | OA (one) |
| Beijing | Pixel-level | 89.5 ± 1.5 | 88.2 ± 1.1 | 88.8 ± 1.1 | 69.8 ± 2.3 | 93.2 ± 1.5 |
| | Object-level | 92.5 ± 1.0 | 88.1 ± 1.1 | 90.2 ± 0.8 | 68.9 ± 2.0 | 93.0 ± 1.5 |
| Shanghai | Pixel-level | 90.6 ± 1.3 | 89.5 ± 1.0 | 90.0 ± 0.9 | 78.2 ± 1.3 | 92.8 ± 0.6 |
| | Object-level | 94.3 ± 1.1 | 88.7 ± 1.3 | 91.4 ± 0.9 | 77.1 ± 1.3 | 92.3 ± 0.9 |

evaluated the accuracies of the proposed method. Specifically, we divided the study areas into 5 km by 5 km grids, and then, we randomly generated and labeled a number of samples (in pixels) for each grid. The minimum distance between samples was set to 100 $m$ to avoid the spatial autocorrelation. In this way, we collected 500 NCBA pixels and 500 non-NCBA pixels. Moreover, we repeated the aforementioned sampling procedure ten-times, and generated 10 groups of sample sets and calculated the mean and standard derivation for accuracy assessment.

Table 6 show the accuracies of NCBAs and change timing with both pixel-level and object-level assessment. Regarding the detection accuracy, the pixel-level samples achieved slightly lower F-score values than the object-level samples. However, with respect to the change timing, the pixel-level samples gave higher OAs than the object-based ones with both exact match and one-year tolerance strategies. This phenomenon is possibly due to the factor that the planar and vertical features adopted in this research are calculated in a local neighborhood, leading to higher accuracy for the change detection but lower accuracy for the change timing at the object level.

In addition, we compared the results using the nadir panchromatic images and the brightness images as the basis for feature extraction. The brightness images (the maximum of visible bands for each pixel) were selected according to the relevant literature (Huang and Zhang, 2012; Pesaresi et al., 2011), considering that the visible bands contribute most to the spectral information of buildings. As shown in Table 7, we can observe that there is little difference between the two types of base images in terms of the accuracies of NCBAs and change timing.

### 5.2. Performance of the object-based temporal correction

The object-based temporal correction is used for improving the spatiotemporal consistency of the features. To investigate its performance, we analyzed the effect of the segmentation scale and the temporal correction. Firstly, we compared temporal correction at the pixel level and the object level, where four segmentation scales (i.e., 25, 50, 75, and 100) were considered (Table 8). In general, the object level outperforms the pixel level in terms of the accuracies of the NCBA detection and change timing, and the object level improves the mean F-score value of the NCBAs and the mean OA of the change timing, in both study areas. At the object level, scales 25 and 50 achieve slightly higher mean F-score values for the NCBA detection than scales 75 and

100, and regarding the change timing, scales 50, 75, and 100 obtain slightly higher mean overall accuracies than scale 25, in both study areas. However, in general, the results across different segmentation scales do not show much oscillation, indicating that the proposed method is robust. Note that a small scale is preferable to a large one, since the latter can easily lead to under-segmentation and loss of details. Therefore, it was reasonable to set the segmentation scale as 50 in this study.

We also compared the object-based features (at the segmentation scale of 50) with and without temporal correction, and forward and backward correction directions as well as their average were considered. As shown in Table 9, in the four situations, the temporal correction with the average of two directions performs the best, and the backward correction performs the worst, in terms of the F-score values of NCBAs and the overall accuracies of change timing. These results verify the effectiveness of the average backward-forward temporal correction.

Fig. 9 presents an example of the multi-temporal features with and without object-based temporal correction, with the average of forward and backward directions adopted. It can be seen that the object-based temporal correction suppresses the salt-and-pepper effect induced by the heterogeneity of the high-resolution images. At the same time, it removes temporal outliers and retains true changes, e.g., the NCBAs in the bottom-right corner. In addition, the joint use of planar-vertical features also has the potential to suppress the uncertainty of observations. Note that temporal correction is based on the assumption that urban land expansion is commonly irreversible during a short time period (Schneider, 2012). However, when the temporal period is expanded to a longer one (e.g., decades), building reconstruction is likely to occur in urban area. Particularly, for most of cases of reconstruction, i.e., the conversion of low-rise building areas to middle-high building areas, our approach can detect it due to the high response of planar-vertical features, such as sites 3 and 8 in Fig. 6.

### 5.3. Performance of the multi-temporal change detection

Since 1972, Landsat satellites have collected a large number of optical images with a spatial resolution of 30–60 m and a temporal resolution of 16 days (Wulder et al., 2019). With the open data access policy (Woodcock et al., 2008), Landsat images have been widely applied to land cover change monitoring (Gong et al., 2019; X. Li et al., 2015; Schneider, 2012). However, Landsat images cannot detect

**Table 7**

Comparison of the accuracies (%) of NCBAs and change timing obtained by the nadir panchromatic images (PAN) and the brightness images (BT) in Beijing and Shanghai. UA: user's accuracy; PA: producer's accuracy; OA: overall accuracy; exact: exact match; one: one-year tolerance.

| | | NCBAs | | | Change timing | |
|---|---|---|---|---|---|---|
| | | UA | PA | F-score | OA (exact) | OA (one) |
| Beijing | PAN | 92.5 ± 1.0 | 88.1 ± 1.1 | 90.2 ± 0.8 | 68.9 ± 2.0 | 93.0 ± 1.5 |
| | BT | 92.5 ± 0.9 | 88.3 ± 1.6 | 90.4 ± 1.1 | 68.7 ± 1.8 | 92.9 ± 1.3 |
| Shanghai | PAN | 94.3 ± 1.1 | 88.7 ± 1.3 | 91.4 ± 0.9 | 77.1 ± 1.3 | 92.3 ± 0.9 |
| | BT | 94.4 ± 0.9 | 88.5 ± 1.4 | 91.3 ± 0.9 | 77.3 ± 1.1 | 92.2 ± 1.0 |

**Table 8**
The accuracies (%) of the NCBAs and their change timings at the pixel level and the object level, where four segmentation scales were considered. UA: user's accuracy; PA: producer's accuracy; OA: overall accuracy; exact: exact match; one: one-year tolerance.

| | | | Pixel level | Object level | | | |
|---|---|---|---|---|---|---|---|
| | | | | 25 | 50 | 75 | 100 |
| Beijing | NCBAs | UA | 93.4 ± 0.7 | 92.7 ± 0.9 | 92.5 ± 1.0 | 92.1 ± 0.7 | 91.9 ± 0.7 |
| | | PA | 78.9 ± 1.4 | 87.3 ± 1.4 | 88.1 ± 1.1 | 86.8 ± 1.5 | 85.4 ± 1.8 |
| | | F-score | 85.6 ± 0.9 | 89.9 ± 1.0 | 90.2 ± 0.8 | 89.4 ± 0.8 | 88.5 ± 1.2 |
| | Change timing | OA (exact) | 61.0 ± 1.7 | 66.5 ± 1.7 | 68.9 ± 2.0 | 69.1 ± 1.5 | 69.9 ± 1.5 |
| | | OA (one) | 87.5 ± 1.7 | 91.8 ± 1.3 | 93.0 ± 1.5 | 93.1 ± 1.4 | 92.7 ± 1.6 |
| Shanghai | NCBAs | UA | 95.8 ± 0.7 | 94.6 ± 0.9 | 94.3 ± 1.1 | 94.4 ± 0.8 | 93.8 ± 0.6 |
| | | PA | 80.4 ± 1.5 | 87.5 ± 1.0 | 88.7 ± 1.3 | 87.9 ± 1.4 | 86.3 ± 1.5 |
| | | F-score | 87.4 ± 1.1 | 90.9 ± 0.8 | 91.4 ± 0.9 | 91.0 ± 1.1 | 89.9 ± 0.9 |
| | Change timing | OA (exact) | 67.7 ± 2.2 | 75.2 ± 2.2 | 77.1 ± 1.3 | 78.8 ± 1.3 | 78.2 ± 1.8 |
| | | OA (one) | 88.0 ± 1.4 | 91.6 ± 1.1 | 92.3 ± 0.9 | 92.8 ± 1.1 | 92.8 ± 1.4 |

vertical changes, and meanwhile, they often suffer from the problem of mixed pixels due to the limitation of the spatial resolution. By contrast, the multi-view ZY-3 images, containing 2.1-m nadir-view, 2.5–3.5-m forward/backward-view ( ± 22°), and 5.8-m multispectral images, can provide: 1) rich spatial details for clearly delineating ground objects and 2) vertical features for describing 3D urban morphology. In this context, the time series of ZY-3 images make it possible to characterize both 2D and 3D change patterns of ground objects at a fine spatial scale.

With respect to high-resolution change detection, most of the existing studies have focused on bi-temporal images. However, multi-temporal images can provide more abundant time-series information than bi-temporal ones. The time-series information can indicate both where and when changes occur, which is vital for a thorough understanding of urban expansion. The proposed multi-temporal change detection method analyzed the distinctive temporal pattern of NCBAs and simultaneously captured the change positions and timings using the time series of ZY-3 images. In this section, three issues were discussed: 1) to evaluate the performance of the proposed method, we compared it with a multi-temporal regression method; 2) we investigated the effect of time-series information on detecting NCBAs by comparing the proposed method with a bi-temporal method; and 3) we analyzed the effect of inconsistent temporal information on monitoring NCBAs.

Firstly, we applied the state-of-the-art multi-temporal regression method developed by Li et al. (2018), since it is very effective in identifying urbanized areas and the change timings by analyzing the regression lines of three indicators derived from Landsat images, i.e., the normalized difference vegetation index (NDVI), the modified normalized difference water index (MNDWI), and the short-wave infrared (SWIR) band. However, since our research focused on the detection of NCBAs with high-resolution images, we could not directly employ these three indicators in the experiments. Therefore, to ensure a fair comparison between the proposed method and the multi-temporal regression method, the same input features were used, i.e., the planar-vertical features with object-based temporal correction. As illustrated in

Table 10, the two methods obtain comparable accuracies for detecting NCBAs in both study areas. However, the proposed method performs slightly better in capturing the change timing. The mean overall accuracies with the exact match and the one-year tolerance strategies are improved by 6.0% and 1.7% for Beijing, respectively, and 8.1% and 1.1% for Shanghai, respectively. Note that the two methods were initially designed for different indicators relevant to different application scenarios, which can explain the discrepancies in performance.

Fig. 10 further displays the histograms of the difference between the detected change timings (by the two methods) and the reference change timings. Compared to the multi-temporal regression method (Li et al., 2018), the proposed method detects more exact matches of change timing. In addition, most of the change timings detected by the two methods are concentrated in the neighboring years. The main reason for the confusion is that: amount of building construction would take several years to complete, but some of planar or vertical features may have a significant response before (i.e., conversion of bare soil to paved surface) and under construction, owing to the rich details provided by ZY-3 images. Overall, these results demonstrate the strengths of the proposed method, especially for determining the change timings of NCBAs.

In addition, we implemented the bi-temporal method with only two image sets (acquired on the first and last dates, respectively) to calculate the change magnitude, for a comparison with the proposed multi-temporal method (see Section 3.4). Fig. 11 shows the accuracy increment obtained by the multi-temporal method in NCBA detection, and the effect of the different feature combinations is also shown. When the planar features or the planar-vertical fusion features are used, the multi-temporal method considerably increases the F-score values, compared to adopting only the bi-temporal images (acquired on the first and last dates). This can be attributed to the fact that planar features are sensitive to the uncertainties caused by poor image quality (e.g., noise induced by complicated imaging conditions). Nevertheless, this deficiency can be effectively compensated by the consideration of the time-

**Table 9**
The accuracies (%) of the NCBAs and their change timings with and without temporal correction, where forward and backward correction directions as well as their average were considered. UA: user's accuracy; PA: producer's accuracy; OA: overall accuracy; exact: exact match; one: one-year tolerance.

| | | NCBAs | | | Change timing | |
|---|---|---|---|---|---|---|
| | | UA | PA | F-score | OA (exact) | OA (one) |
| Beijing | Without | 92.7 ± 0.9 | 84.0 ± 0.7 | 88.1 ± 0.5 | 64.0 ± 2.0 | 87.5 ± 1.7 |
| | Forward | 90.6 ± 0.8 | 87.2 ± 1.4 | 88.8 ± 0.9 | 67.9 ± 2.3 | 91.9 ± 1.7 |
| | Backward | 90.6 ± 0.9 | 82.3 ± 1.4 | 86.2 ± 1.1 | 60.8 ± 0.8 | 85.1 ± 0.8 |
| | Average | 92.5 ± 1.0 | 88.1 ± 1.1 | 90.2 ± 0.8 | 68.9 ± 2.0 | 93.0 ± 1.5 |
| Shanghai | Without | 94.9 ± 1.1 | 84.3 ± 0.8 | 89.3 ± 0.7 | 73.7 ± 1.8 | 89.6 ± 1.0 |
| | Forward | 93.9 ± 1.0 | 88.8 ± 1.5 | 91.3 ± 1.0 | 75.7 ± 1.4 | 92.9 ± 0.8 |
| | Backward | 93.2 ± 1.0 | 76.0 ± 1.3 | 83.7 ± 1.0 | 71.6 ± 1.6 | 86.9 ± 1.7 |
| | Average | 94.3 ± 1.1 | 88.7 ± 1.3 | 91.4 ± 0.9 | 77.1 ± 1.3 | 92.3 ± 0.9 |
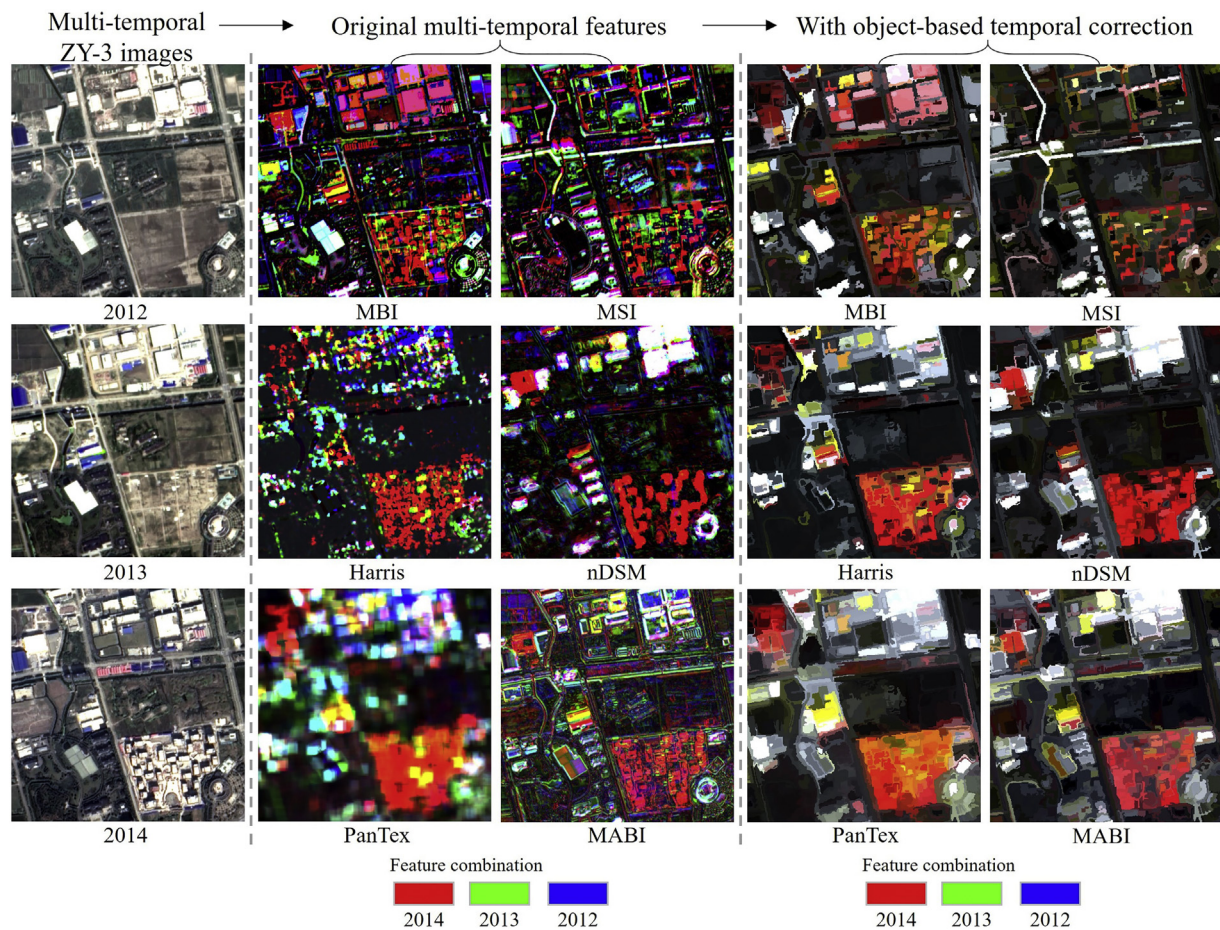
**Fig. 9.** An example (1 km by 1 km) of the multi-temporal features with and without object-based temporal correction, with the average of forward and backward directions adopted in Shanghai. Multi-temporal features in 2014, 2013, and 2012 are displayed in red, green, and blue, respectively. (For interpretation of the references to colour in this figure legend, the reader is referred to the web version of this article.)

series information. Moreover, it can be seen that the multi-temporal images have little impact on nDSM and MABI, showing that the multi-view features are very effective for detecting NCBAs. Meanwhile, it should be kept in mind that the bi-temporal method cannot determine the change timing, owing to the absence of time-series information.

Fig. 12 displays an example of the NCBAs obtained by the multi-temporal and bi-temporal methods for different feature combinations. It can be seen that, compared to the bi-temporal method, the multi-temporal method captures more complete NCBAs dominated by low-rise dark buildings, such as the dense new residential area (site 1) with the fused planar features, and the large new warehouse (site 2) with the fused vertical features. This phenomenon indicates that the time-series information inherent in multi-temporal images has the ability to improve the performance of both planar and vertical features. In addition, it can be seen that the planar and vertical features effectively complement each other, which validates the reliability of their joint use in

identifying complex and diverse NCBAs.

In addition, we compared the results of consistent and inconsistent temporal information on monitoring NCBAs. Specifically, the consistent result was generated by using one image set for each year at similar acquisition time, while the inconsistent result was obtained by using all the available images (i.e., a total of 14 image sets in Beijing and 8 image sets in Shanghai). Our results (Table 11) show that there is little difference between the consistent and inconsistent approaches, in terms of the accuracies of NCBAs and change timing. The reasons can be possibly attributed to the following two aspects: On the one hand, NCBAs usually exhibit less seasonal fluctuation than vegetation, and the planar-vertical features can directly indicate the presence of building areas, rather than non-building areas (e.g., bare soil and vegetation). On the other hand, the joint use of planar-vertical features and object-based temporal correction can suppress the effect of inconsistent temporal information.

**Table 10**

Comparison of the accuracies (%) of the NCBAs and their change timings between the proposed method and the multi-temporal regression method of Li et al. (2018). UA: user's accuracy; PA: producer's accuracy; OA: overall accuracy; exact: exact match; one: one-year tolerance.

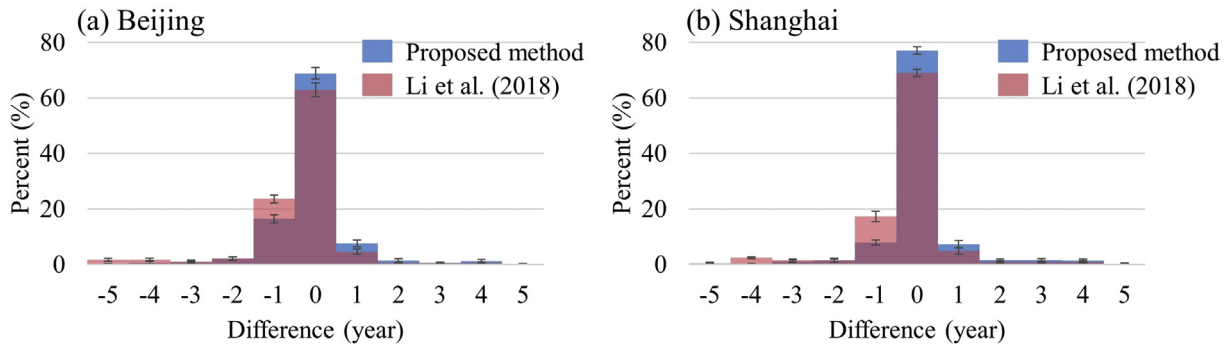| | | NCBAs | | | Change timing | |
|---|---|---|---|---|---|---|
| | | UA | PA | F-score | OA (exact) | OA (one) |
| Beijing | Proposed method | 92.5 ± 1.0 | 88.1 ± 1.1 | 90.2 ± 0.8 | 68.9 ± 2.0 | 93.0 ± 1.5 |
| | Li et al. (2018) | 92.4 ± 1.0 | 87.4 ± 1.2 | 89.8 ± 0.8 | 62.9 ± 2.4 | 91.3 ± 1.4 |
| Shanghai | Proposed method | 94.3 ± 1.1 | 88.7 ± 1.3 | 91.4 ± 0.9 | 77.1 ± 1.3 | 92.3 ± 0.9 |
| | Li et al. (2018) | 94.5 ± 1.0 | 87.6 ± 1.0 | 90.9 ± 0.7 | 69.0 ± 1.2 | 91.2 ± 0.9 |

**Fig. 10.** Histograms of the difference between the detected change timings (by the proposed method and the multi-temporal regression method of Li et al. (2018)) and the reference change timings.

### 5.4. Implications for land resource management

This research provided two major implications for land resource management:

Firstly, the proposed automated approach can achieve high accuracy for detecting NCBAs (with F-score of about 90%), and the false alarms (6–8%) can be further filtered out with slight human intervention. However, at the patch level, 73 out of 1344 (5.4%) NCBAs were completely missed for Beijing, while 42 out of 954 (4.4%) for Shanghai. Most of the missed NCBAs corresponded to one individual or several buildings, and they were usually small and low (e.g., temporary buildings), which were not well characterized by the planar-vertical features owing to their low response. In addition, the proposed approach can be used as early warning for land resource management. For instance, attention should be paid to the areas with significant changes of texture or structure, since these changes often indicate building construction.

Secondly, some of the planar or vertical features can have a significant response before (i.e., conversion of bare soil to paved surface) or under the construction of building areas, owing to the rich details provided by ZY-3 images. This is useful for early warning for the emergence of NCBAs. In addition, please kindly notice that, although it is difficult to accurately identify the change timing of NCBAs, the time-series images have the potential to improve the performance of planar-vertical features on detecting their presence and spatial extent.

### 6. Conclusions

In this paper, we focused on monitoring NCBAs and their change timing with the time series of ZY-3 images. Concerning the method, we proposed a series of original algorithms:

#### 6.1. Multi-temporal high-resolution image change detection method

Most of existing high-resolution change detection studies used bi-

temporal images, which may lead to a large number of false alarms owing to the uncertainty of complicated imaging conditions. In this research, therefore, we used multi-temporal images to overcome this issue, by proposing an object-based temporal correction for improving the spatial-temporal consistency, and an automatic multi-temporal change detection algorithm for detecting NCBAs and their change timing.

#### 6.2. Nadir-based high-resolution change detection

In particular, most of existing high-resolution change detection studies are not based on nadir images, and thereby are subject to spurious changes induced by different viewing angles. In this regard, this research used the nadir images as the baselines to suppress this effect.

#### 6.3. A comprehensive fusion of time-series 2D and 3D features

We systematically integrated 2D and 3D feature sets (2D: MBI, Harris, PanTex; 3D: MSI, nSDM, MABI). The additional 3D features, i.e., MSI and nDSM, have not been considered by previous research (Liu et al., 2019), but were proven effective in this study. MSI (morphological shadow index) can indicate the height of buildings by measuring the structure of shadows (Huang and Zhang, 2012). The nDSM (normalized Digital Surface Model) can describe 3D information of building areas by utilizing the stereo matching technique (Qin and Fang, 2014).

We tested the proposed method on two urban fringe areas of Beijing (7 multi-temporal image sets) and Shanghai (7 multi-temporal image sets), respectively, where rapid urbanization is taking place. The major conclusions are summarized below:

1) The planar-vertical features extracted from the multi-view ZY-3 images can delineate NCBAs from different perspectives by feature fusion. Specifically, multi-view features (i.e., nDSM and MABI) are effective for detecting NCBAs and capturing their change timings.
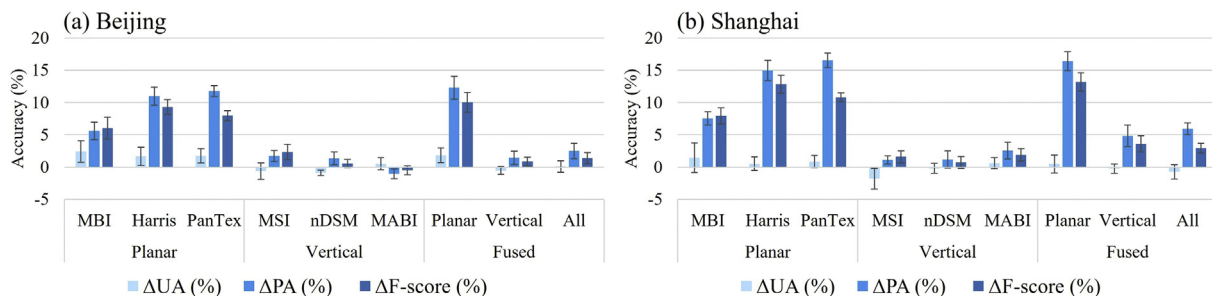


**Fig. 11.** The accuracy increment obtained by the multi-temporal method compared to the bi-temporal method, in terms of NCBA detection. All: the planar-vertical features; UA: user's accuracy; PA: producer's accuracy; Δ: the accuracy increment.
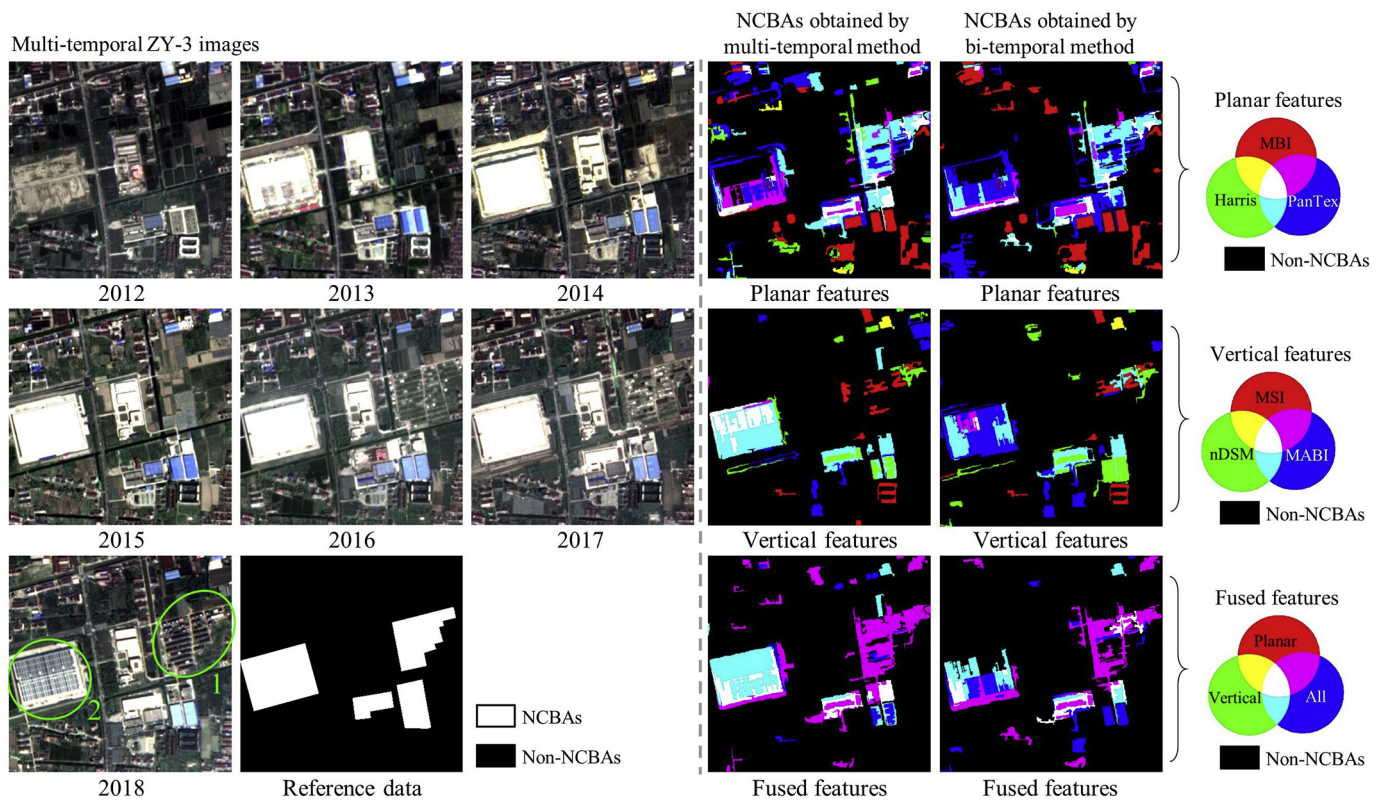
**Fig. 12.** An example (1 km by 1 km) of the NCBAs obtained by the multi-temporal and bi-temporal methods for different feature combinations in Shanghai.

2) The object-based temporal correction is able to mitigate the heterogeneity of high-resolution images and remove temporal noise, and can thus improve the spatiotemporal consistency of the features.

3) The proposed multi-temporal change detection method shows a satisfactory performance, with an F-score value of about 90% in detecting NCBAs, and an OA of around 92% in identifying change timings using the one-year tolerance strategy.

4) We found that, compared to bi-temporal images, multi-temporal images can greatly enhance the performance of the planar features and the planar-vertical fusion features. However, the time-series information barely affects the performance of the multi-view features, verifying their effectiveness for NCBA detection. Moreover, it should be kept in mind that the change timing cannot be identified without multi-temporal images.

There are some limitations to the proposed automated method. For instance, it may falsely detect rebuilt building areas, though such changes rarely happen. However, these errors can be filtered out through the existing NCBA databases. Moreover, due to the limitation of the ZY-3 data acquisition ability, we cannot obtain more dense times-series images, and hence the seasonal information from the ZY-3 constellation, which is useful for further eliminating some false alarms, is not sufficient. Nevertheless, considering that this research focused on

building areas, which exhibit less seasonal fluctuation than vegetation, the negative effects caused by the limited data availability were not so apparent. The proposed automated approach yielded satisfactory results on two study areas (Beijing and Shanghai). However, for areas where only few changes happen, the approach still holds potential. The main reason is that the approach uses planar-vertical features for lowering the uncertainty of a single feature, and considers multi-temporal observations for alleviating the instability of a single observation (e.g., noise induced by complicated imaging conditions). Therefore, it's potential to apply the approach to less dynamic areas in future work. In addition, this research focused on a very specific issue, i.e., monitoring NCBAs for protecting arable land and ecosystem in the context of the rapid urbanization of China. In future work, to extend the current research, we plan to investigate the conversion sources of NCBAs, e.g., croplands, forest, wetland.

## CRediT authorship contribution statement

**Xin Huang:** Conceptualization, Methodology, Writing - original draft, Writing - review & editing. **Yinxia Cao:** Software, Writing - original draft, Writing - review & editing. **Jiayi Li:** Methodology.

**Table 11**

Comparison of the accuracies (%) of NCBAs and change timing between the consistent and inconsistent results. UA: user's accuracy; PA: producer's accuracy; OA: overall accuracy; exact: exact match; one: one-year tolerance.

| | | NCBAs | | | Change timing | |
|---|---|---|---|---|---|---|
| | | UA | PA | F-score | OA (exact) | OA (one) |
| Beijing | Consistent | 92.5 ± 1.0 | 88.1 ± 1.1 | 90.2 ± 0.8 | 68.9 ± 2.0 | 93.0 ± 1.5 |
| | Inconsistent | 91.6 ± 1.0 | 88.5 ± 1.2 | 90.0 ± 0.9 | 66.5 ± 1.7 | 93.0 ± 1.1 |
| Shanghai | Consistent | 94.3 ± 1.1 | 88.7 ± 1.3 | 91.4 ± 0.9 | 77.1 ± 1.3 | 92.3 ± 0.9 |
| | Inconsistent | 94.2 ± 1.2 | 88.5 ± 1.2 | 91.3 ± 1.0 | 77.1 ± 1.8 | 92.4 ± 0.8 |

## Declaration of competing interest

## References

Baatz, M., Schäpe, A., 2000. Multiresolution Segmentation: An Optimization Approach for High Quality Multi-Scale Image Segmentation. Angewandte Geographische Informationsverarbeitung, pp. 12–23.

Bai, Y., Jiang, B., Wang, M., Li, H., Alatalo, J.M., Huang, S., 2016. New ecological redline policy (ERP) to secure ecosystem services in China. Land Use Policy 55, 348–351. https://doi.org/10.1016/j.landusepol.2015.09.002.

Balk, D.L., Nghiem, S.V., Jones, B.R., Liu, Z., Dunn, G., 2019. Up and out: a multifaceted approach to characterizing urbanization in Greater Saigon, 2000–2009. Landsc. Urban Plan. 187, 199–209. https://doi.org/10.1016/j.landurbplan.2018.07.009.

Ban, Y., Yousif, O.A., 2012. Multitemporal spaceborne SAR data for urban change detection in China. IEEE J. Sel. Top. Appl. Earth Obs. Remote Sens. 5, 1087–1094. https://doi.org/10.1109/JSTARS.2012.2201135.

Ban, Y., Webber, L., Gamba, P., Paganini, M., 2017. EO4Urban: sentinel-1A SAR and sentinel-2A MSI data for global urban services. In: 2017 Joint Urban Remote Sensing Event, JURSE 2017. Institute of Electrical and Electronics Engineers Inc. https://doi.org/10.1109/JURSE.2017.7924550.

Benedetti, A., Picchiani, M., Del Frate, F., 2018. Sentinel-1 and sentinel-2 data fusion for urban change detection. In: Int. Geosci. Remote Sens. Symp. 2018-July, 1962–1965, https://doi.org/10.1109/IGARSS.2018.8517586.

Bouziani, M., Goïta, K., He, D.-C., 2010. Automatic change detection of buildings in urban environment from very high spatial resolution images using existing geodatabase and prior knowledge. ISPRS J. Photogramm. Remote Sens. 65, 143–153. https://doi.org/10.1016/j.isprsjprs.2009.10.002.

Bovolo, F., 2009. A multilevel parcel-based approach to change detection in very high resolution multitemporal images. IEEE Geosci. Remote Sens. Lett. 6, 33–37. https://doi.org/10.1109/LGRS.2008.2007429.

Bovolo, F., Bruzzone, L., 2007. A theoretical framework for unsupervised change detection based on change vector analysis in the polar domain. IEEE Trans. Geosci. Remote Sens. 45, 218–236. https://doi.org/10.1109/TGRS.2006.885408.

Bren d'Amour, C., Reitsma, F., Baiocchi, G., Barthel, S., Güneralp, B., Erb, K.-H., Haberl, H., Creutzig, F., Seto, K.C., 2017. Future urban land expansion and implications for global croplands. Proc. Natl. Acad. Sci. 114, 8939–8944. https://doi.org/10.1073/pnas.1606036114.

Bruzzone, L., Bovolo, F., 2013. A novel framework for the design of change-detection systems for very-high-resolution remote sensing images. Proc. IEEE 101, 609–630. https://doi.org/10.1109/JPROC.2012.2197169.

Celik, T., Ma, K.K., 2011. Multitemporal image change detection using undecimated discrete wavelet transform and active contours. IEEE Trans. Geosci. Remote Sens. 49, 706–716. https://doi.org/10.1109/TGRS.2010.2066979.

Chaabouni-Chouayakh, H., Reinartz, P., 2011. Towards automatic 3D change detection inside urban areas by combining height and shape information. Photogramm. Fernerkundung, Geoinf. 2011, 205–217. https://doi.org/10.1127/1432-8364/2011/0083.

Che, M., Du, P., Gamba, P., 2018. 2- and 3-D urban change detection with quad-PolSAR data. IEEE Geosci. Remote Sens. Lett. 15, 68–72. https://doi.org/10.1109/LGRS.2017.2773471.

Chen, G., Hay, G.J., Carvalho, L.M.T., Wulder, M.A., 2012. Object-based change detection. Int. J. Remote Sens. https://doi.org/10.1080/01431161.2011.648285.

ChinaDaily, 2015. China investigates almost 40,000 cases of land misuse [WWW document]. URL. http://europe.chinadaily.com.cn/china/2015-09/15/content_21885562.htm, Accessed date: 26 April 2019.

ChinaDaily, 2017. China to launch third national land survey [WWW document]. URL. http://www.chinadaily.com.cn/china/2017-10/16/content_33334326.htm, Accessed date: 17 December 2019.

ChinaDaily, 2019. High-resolution satellite imagery used in China's land survey [WWW document]. URL. http://www.chinadaily.com.cn/a/201908/16/WS5d566a7da310cf3e3556639f.html, Accessed date: 17 December 2019.

Cohen, B., 2011. Urban growth in developing countries: a review of current trends and a caution regarding existing forecasts. World Dev. https://doi.org/10.1016/j.worlddev.2003.04.008.

Coppin, P., Jonckheere, I., Nackaerts, K., Muys, B., Lambin, E., 2004. Digital change detection methods in ecosystem monitoring: a review. Int. J. Remote Sens. 25, 1565–1596. https://doi.org/10.1080/0143116031000101675.

Del Frate, F., Pacifici, F., Solimini, D., 2008. Monitoring urban land cover in Rome, Italy, and its changes by single-polarization multitemporal SAR images. IEEE J. Sel. Top. Appl. Earth Obs. Remote Sens. 1, 87–97. https://doi.org/10.1109/JSTARS.2008.2002221.

Drusch, M., Del Bello, U., Carlier, S., Colin, O., Fernandez, V., Gascon, F., Hoersch, B., Isola, C., Laberinti, P., Martimort, P., Meygret, A., Spoto, F., Sy, O., Marchese, F., Bargellini, P., 2012. Sentinel-2: ESA's optical high-resolution Mission for GMES operational services. Remote Sens. Environ. 120, 25–36. https://doi.org/10.1016/j.rse.2011.11.026.

Falco, N., Mura, M.D., Bovolo, F., Benediktsson, J.A., Bruzzone, L., 2013. Change detection in VHR images based on morphological attribute profiles. IEEE Geosci. Remote Sens. Lett. 10, 636–640. https://doi.org/10.1109/LGRS.2012.2222340.

Fei, W., Zhao, S., 2019. Urban land expansion in China's six megacities from 1978 to 2015. Sci. Total Environ. 664, 60–71.

Fratarcangeli, F., Murchio, G., Di Rita, M., Nascetti, A., Capaldo, P., 2016. Digital surface models from ZiYuan-3 triplet: performance evaluation and accuracy assessment. Int. J. Remote Sens. 37, 3505–3531. https://doi.org/10.1080/01431161.2016.1192308.

Fu, P., Weng, Q., 2016. A time series analysis of urbanization induced land use and land cover change and its impact on land surface temperature with Landsat imagery. Remote Sens. Environ. 175, 205–214. https://doi.org/10.1016/J.RSE.2015.12.040.

Gamba, P., Houshmand, B., 2000. Digital surface models and building extraction: a comparison of IFSAR and LIDAR data. IEEE Trans. Geosci. Remote Sens. 38, 1959–1968. https://doi.org/10.1109/36.851777.

Gamba, P., Dell'Acqua, F., Lisini, G., 2006. Change detection of multitemporal SAR data in urban areas combining feature-based and pixel-based techniques. IEEE Trans. Geosci. Remote Sens. 44, 2820–2827. https://doi.org/10.1109/TGRS.2006.879498.

Gamba, P., Dell'Acqua, F., Trianni, G., 2007. Rapid damage detection in the bam area using multitemporal SAR and exploiting ancillary data. IEEE Trans. Geosci. Remote Sens. 45, 1582–1589. https://doi.org/10.1109/TGRS.2006.885392.

Gong, P., Li, X., Zhang, W., 2019. 40-year (1978–2017) human settlement changes in China reflected by impervious surfaces from satellite remote sensing. Sci. Bull. 64, 756–763. https://doi.org/10.1016/j.scib.2019.04.024.

Gonzalez, R.C., Woods, R.E., 2002. Digital Image Processing, second. ed. (Prentice Hall).

Grey, W.M.F., Luckman, A.J., Holland, D., 2003. Mapping urban change in the UK using satellite radar interferometry. Remote Sens. Environ. 87, 16–22. https://doi.org/10.1016/S0034-4257(03)00142-1.

Guerin, C., Binet, R., Pierrot-Deseilligny, M., 2014. Automatic detection of elevation changes by differential DSM analysis: application to urban areas. IEEE J. Sel. Top. Appl. Earth Obs. Remote Sens. 7, 4020–4037. https://doi.org/10.1109/JSTARS.2014.2300509.

Haas, J., Ban, Y., 2018. Urban land cover and ecosystem service changes based on sentinel-2A MSI and Landsat TM data. IEEE J. Sel. Top. Appl. Earth Obs. Remote Sens. 11, 485–497. https://doi.org/10.1109/JSTARS.2017.2786468.

Harris, C., Stephens, M., 1988. A combined corner and edge detector. In: Alvey Vision Conference, pp. 10–5244. https://doi.org/10.5244/C.2.23.

He, C., Liu, Z., Tian, J., Ma, Q., 2014. Urban expansion dynamics and natural habitat loss in China: a multiscale landscape perspective. Glob. Chang. Biol. 20, 2886–2902. https://doi.org/10.1111/gcb.12553.

He, C., Gao, B., Huang, Q., Ma, Q., Dou, Y., 2017. Environmental degradation in the urban areas of China: evidence from multi-source remote sensing data. Remote Sens. Environ. 193, 65–75. https://doi.org/10.1016/j.rse.2017.02.027.

Hirschmüller, H., 2008. Stereo processing by semiglobal matching and mutual information. IEEE Trans. Pattern Anal. Mach. Intell. 30, 328–341. https://doi.org/10.1109/TPAMI.2007.1166.

Hu, H., Ban, Y., 2014. Unsupervised change detection in multitemporal SAR images over large urban areas. IEEE J. Sel. Top. Appl. Earth Obs. Remote Sens. 7, 3248–3261. https://doi.org/10.1109/JSTARS.2014.2344017.

Hu, T., Huang, X., 2019. A novel locally adaptive method for modeling the spatiotemporal dynamics of global electric power consumption based on DMSP-OLS nighttime stable light data. Appl. Energy 240, 778–792.

Huang, X., Zhang, L., 2011. A multidirectional and multiscale morphological index for automatic building extraction from multispectral geo eye-1 imagery. Photogramm. Eng. Remote. Sens. 77, 721–732. https://doi.org/10.14358/PERS.77.7.721.

Huang, X., Zhang, L., 2012. Morphological building/shadow index for building extraction from high-resolution imagery over urban areas. IEEE J. Sel. Top. Appl. Earth Obs. Remote Sens. 5, 161–172. https://doi.org/10.1109/JSTARS.2011.2168195.

Huang, C., Goward, S.N., Masek, J.G., Thomas, N., Zhu, Z., Vogelmann, J.E., 2010. An automated approach for reconstructing recent forest disturbance history using dense Landsat time series stacks. Remote Sens. Environ. 114, 183–198. https://doi.org/10.1016/j.rse.2009.08.017.

Huang, X., Wen, D., Li, J., Qin, R., 2017. Multi-level monitoring of subtle urban changes for the megacities of China using high-resolution multi-view satellite imagery. Remote Sens. Environ. 196, 56–75. https://doi.org/10.1016/j.rse.2017.05.001.

Hussain, M., Chen, D., Cheng, A., Wei, H., Stanley, D., 2013. Change detection from remotely sensed images: from pixel-based to object-based approaches. ISPRS J. Photogramm. Remote Sens. 80, 91–106. https://doi.org/10.1016/j.isprsjprs.2013.03.006.

Im, J., Jensen, J.R., Tullis, J.A., 2008. Object-based change detection using correlation image analysis and image segmentation. Int. J. Remote Sens. 29, 399–423. https://doi.org/10.1080/01431160601075582.

Inglacla, J., Mercier, G., 2007. A new statistical similarity measure for change detection in multitemporal SAR images and its extension to multiscale change analysis. IEEE Trans. Geosci. Remote Sens. 45, 1432–1445. https://doi.org/10.1109/TGRS.2007.893568.

Jian, L., Zhiyang, Q., Zijun, Y., 2017. "Delimitation" and "implementation" of urban growth boundary:analysis and thoughts on the practice in 14 pilot cities in China.

Urban Plan. Forum. https://doi.org/10.16361/j.upf.201702004.

Kennedy, R.E., Cohen, W.B., 2003. Automated designation of tie-points for image-to-image coregistration. Int. J. Remote Sens. 24, 3467–3490. https://doi.org/10.1080/0143116021000024249.

Kennedy, R.E., Yang, Z., Cohen, W.B., 2010. Detecting trends in forest disturbance and recovery using yearly Landsat time series: 1. LandTrendr - temporal segmentation algorithms. Remote Sens. Environ. 114, 2897–2910. https://doi.org/10.1016/j.rse.2010.07.008.

Kong, X., 2014. China must protect high-quality arable land. Nature. https://doi.org/10.1038/506007a.

Laben, C.A., Brower, B.V., 2000. Process for Enhancing the Spatial Resolution of Multispectral Imagery Using Pan-Sharpening. US6011875 a.

Lefebvre, A., Corpetti, T., 2017. Monitoring the morphological transformation of Beijing Old City using remote sensing texture analysis. IEEE J. Sel. Top. Appl. Earth Obs. Remote Sens. 10, 539–548. https://doi.org/10.1109/JSTARS.2016.2627545.

Lefebvre, A., Sannier, C., Corpetti, T., 2016. Monitoring urban areas with sentinel-2A data: application to the update of the copernicus high resolution layer imperviousness degree. Remote Sens. 8, 606. https://doi.org/10.3390/rs8070606.

Leichtle, T., Geiß, C., Wurm, M., Lakes, T., Taubenböck, H., 2017. Unsupervised change detection in VHR remote sensing imagery – an object-based clustering approach in a dynamic urban environment. Int. J. Appl. Earth Obs. Geoinf. 54, 15–27. https://doi.org/10.1016/j.jag.2016.08.010.

Li, X., Gong, P., Liang, L., 2015. A 30-year (1984-2013) record of annual urban dynamics of Beijing City derived from Landsat data. Remote Sens. Environ. 166, 78–90. https://doi.org/10.1016/j.rse.2015.06.007.

Li, Y., Yurui, Li, Westlund, H., Liu, Y., 2015. Urban-rural transformation in relation to cultivated land conversion in China: implications for optimizing land use and balanced regional development. Land Use Policy 47, 218–224. https://doi.org/10.1016/j.landusepol.2015.04.011.

Li, X., Zhou, Y., Zhu, Z., Liang, L., Yu, B., Cao, W., 2018. Mapping annual urban dynamics (1985–2015) using time series of Landsat data. Remote Sens. Environ. 216, 674–683.

Li, X., Zhou, Y., Gong, P., Seto, K.C., Clinton, N., 2020. Developing a method to estimate building height from Sentinel-1 data. Remote Sens. Environ. 240, 111705. https://doi.org/10.1016/j.rse.2020.111705.

Liasis, G., Stavrou, S., 2016. Satellite images analysis for shadow detection and building height estimation. ISPRS J. Photogramm. Remote Sens. 119, 437–450. https://doi.org/10.1016/j.isprsjprs.2016.07.006.

Liu, J., Kuang, W., Zhang, Z., Xu, X., Qin, Y., Ning, J., Zhou, W., Zhang, S., Li, R., Yan, C., Wu, S., Shi, X., Jiang, N., Yu, D., Pan, X., Chi, W., 2014. Spatiotemporal characteristics, patterns, and causes of land-use changes in China since the late 1980s. J. Geogr. Sci. 24, 195–210. https://doi.org/10.1007/s11442-014-1082-6.

Liu, Y., Fang, F., Li, Y., 2014. Key issues of land use in China and implications for policy making. Land Use Policy 40, 6–12. https://doi.org/10.1016/j.landusepol.2013.03.013.

Liu, C., Huang, X., Wen, D., Chen, H., Gong, J., 2017. Assessing the quality of building height extraction from ZiYuan-3 multi-view imagery. Remote Sens. Lett. 8, 907–916. https://doi.org/10.1080/2150704X.2017.1335904.

Liu, Y., Ziwen, Z., Zhou, Y., 2018. Efficiency of construction land allocation in China: an econometric analysis of panel data. Land Use Policy 74, 261–272. https://doi.org/10.1016/j.landusepol.2017.03.030.

Liu, C., Huang, X., Zhu, Z., Chen, H., Tang, X., Gong, J., 2019. Automatic extraction of built-up area from ZY3 multi-view satellite imagery: analysis of 45 global cities. Remote Sens. Environ. 226, 51–73. https://doi.org/10.1016/j.rse.2019.03.033.

Marin, C., Bovolo, F., Bruzzone, L., 2015. Building change detection in multitemporal very high resolution SAR images. IEEE Trans. Geosci. Remote Sens. 53, 2664–2682. https://doi.org/10.1109/TGRS.2014.2363548.

Mendez Dominguez, E., Magnard, C., Meier, E., Small, D., Schaepman, M.E., Henke, D., 2019. A back-projection tomographic framework for VHR SAR image change detection. IEEE Trans. Geosci. Remote Sens. 57, 4470–4484. https://doi.org/10.1109/TGRS.2019.2891308.

Mertes, C.M., Schneider, A., Sulla-Menashe, D., Tatem, A.J., Tan, B., 2015. Detecting change in urban areas at continental scales with MODIS data. Remote Sens. Environ. 158, 331–347.

Montazeri, S., Zhu, X.X., Eineder, M., Bamler, R., 2016. Three-dimensional deformation monitoring of urban infrastructure by tomographic SAR using multitrack TerraSAR-X data stacks. IEEE Trans. Geosci. Remote Sens. 54, 6868–6878. https://doi.org/10.1109/TGRS.2016.2585741.

Morisette, J.T., Khorram, S., 2000. Accuracy assessment curves for satellite-based change detection. Photogramm. Eng. Remote Sensing 66, 875–880.

Mura, M.D., Benediktsson, J.A., Bovolo, F., Bruzzone, L., 2008. An unsupervised technique based on morphological filters for change detection in very high resolution images. IEEE Geosci. Remote Sens. Lett. 5, 433–437. https://doi.org/10.1109/LGRS.2008.917726.

NBSC (National Bureau of Statistics of China), 2018. China Statistical Yearbook. China Statistics Press, Beijing.

Olofsson, P., Foody, G.M., Herold, M., Stehman, S.V., Woodcock, C.E., Wulder, M.A., 2014. Good practices for estimating area and assessing accuracy of land change. Remote Sens. Environ. 148, 42–57. https://doi.org/10.1016/j.rse.2014.02.015.

Pacifici, F., Del Frate, F., 2010. Automatic change detection in very high resolution images with pulse-coupled neural networks. IEEE Geosci. Remote Sens. Lett. 7, 58–62. https://doi.org/10.1109/LGRS.2009.2021780.

Pacifici, F., Del Frate, F., Solimini, C., Emery, W.J., 2007. An innovative neural-net method to detect temporal changes in high-resolution optical satellite imagery. IEEE Trans. Geosci. Remote Sens. 45, 2940–2952. https://doi.org/10.1109/TGRS.2007.902824.

Pesaresi, M., Gerhardinger, A., Kayitakire, F., 2008. A robust built-up area presence index by anisotropic rotation-invariant textural measure. IEEE J. Sel. Top. Appl. Earth Obs. Remote Sens. 1, 180–192.

Pesaresi, M., Ehrlich, D., Caravaggi, I., Kauffmann, M., Louvrier, C., 2011. Toward global automatic built-up area recognition using optical VHR imagery. IEEE J. Sel. Top. Appl. Earth Obs. Remote Sens. 4, 923–934. https://doi.org/10.1109/JSTARS.2011.2162579.

Pesaresi, M., Corbane, C., Julea, A., Florczyk, A.J., Syrris, V., Soille, P., 2016. Assessment of the added-value of sentinel-2 for detecting built-up areas. Remote Sens. 8. https://doi.org/10.3390/rs8040299.

Potapov, P.V., Turubanova, S.A., Hansen, M.C., Adusei, B., Broich, M., Altstatt, A., Mane, L., Justice, C.O., 2012. Quantifying forest cover loss in Democratic Republic of the Congo, 2000–2010, with Landsat ETM + data. Remote Sens. Environ. 122, 106–116. https://doi.org/10.1016/j.RSE.2011.08.027.

Powers, D.M.W., 2011. Evaluation: from precision, recall and F-measure to ROC, informedness, markedness and correlation. J. Mach. Learn. Technol. 2, 37–63.

Qin, R., 2014. Change detection on LOD 2 building models with very high resolution spaceborne stereo imagery. ISPRS J. Photogramm. 96, 179–192. https://doi.org/10.1016/j.isprsjprs.2014.07.007.

Qin, R., Fang, W., 2014. A hierarchical building detection method for very high resolution remotely sensed images combined with DSM using graph cut optimization. Photogramm. Eng. Remote Sens. 80, 873–883. https://doi.org/10.14358/PERS.80.9.873.

Qin, R., Tian, J., Reinartz, P., 2016. 3D change detection – approaches and applications. ISPRS J. Photogramm. Remote Sens. https://doi.org/10.1016/j.isprsjprs.2016.09.013.

Ridd, M.K., Liu, J.J., 1998. A comparison of four algorithms for change detection in an urban environment. Remote Sens. Environ. 63, 95–100.

Rowe, N.C., Grewe, L.L., 2001. Change detection for linear features in aerial photographs using edge-finding. IEEE Trans. Geosci. Remote Sens. 39, 1608–1612. https://doi.org/10.1109/36.934092.

SAC (Standardization Administration of the People's Republic of China), 2017. Current Land Use Classification GB/T21010–2017.

Schneider, A., 2012. Monitoring land cover change in urban and peri-urban areas using dense time stacks of Landsat satellite data and a data mining approach. Remote Sens. Environ. 124, 689–704. https://doi.org/10.1016/j.rse.2012.06.006.

Schott, J.R., Salvaggio, C., Volchok, W.J., 1988. Radiometric scene normalization using pseudoinvariant features. Remote Sens. Environ. 26, 1–16. https://doi.org/10.1016/0034-4257(88)90116-2.

Sexton, J.O., Song, X.-P., Huang, C., Channan, S., Baker, M.E., Townshend, J.R., 2013. Urban growth of the Washington, D.C.–Baltimore, MD metropolitan region from 1984 to 2010 by annual, Landsat-based estimates of impervious cover. Remote Sens. Environ. 129, 42–53. https://doi.org/10.1016/j.rse.2012.10.025.

Song, X.-P., Sexton, J.O., Huang, C., Channan, S., Townshend, J.R., 2016. Characterizing the magnitude, timing and duration of urban growth from time series of Landsat-based estimates of impervious cover. Remote Sens. Environ. 175, 1–13. https://doi.org/10.1016/j.rse.2015.12.027.

Stal, C., Tack, F., de Maeyer, P., de Wulf, A., Goossens, R., 2013. Airborne photogrammetry and lidar for DSM extraction and 3D change detection over an urban area - a comparative study. Int. J. Remote Sens. 34, 1087–1110. https://doi.org/10.1080/01431161.2012.717183.

Stehman, S.V., 2012. Impact of sample size allocation when using stratified random sampling to estimate area and area of land-cover change. Remote Sens. Lett. 3, 111–120. https://doi.org/10.1080/01431161.2010.541950.

Su, X., Deledalle, C.A., Tupin, F., Sun, H., 2015. NORCAMA: change analysis in SAR time series by likelihood ratio change matrix clustering. ISPRS J. Photogramm. Remote Sens. 101, 247–261. https://doi.org/10.1016/j.isprsjprs.2014.12.012.

Sun, Y., Zhang, X., Ren, G., Zwiers, F.W., Hu, T., 2016. Contribution of urbanization to warming in China. Nat. Clim. Chang. https://doi.org/10.1038/NCLIMATE2956.

Tang, Y., Zhang, L., Huang, X., 2011. Object-oriented change detection based on the Kolmogorov-Smirnov test using high-resolution multispectral imagery. Int. J. Remote Sens. 32, 5719–5740. https://doi.org/10.1080/01431161.2010.507263.

Taubenböck, H., Esch, T., Felbier, A., Wiesner, M., Roth, A., Dech, S., 2012. Monitoring urbanization in mega cities from space. Remote Sens. Environ. 117, 162–176. https://doi.org/10.1016/j.rse.2011.09.015.

Taubenböck, H., Weigand, M., Esch, T., Staab, J., Wurm, M., Mast, J., Dech, S., 2019. A new ranking of the world's largest cities—do administrative units obscure morphological realities? Remote Sens. Environ. 232. https://doi.org/10.1016/j.rse.2019.111353.

Teo, T.A., Shih, T.Y., 2013. Lidar-based change detection and change-type determination in urban areas. Int. J. Remote Sens. 34, 968–981. https://doi.org/10.1080/01431161.2012.714504.

Tewkesbury, A.P., Comber, A.J., Tate, N.J., Lamb, A., Fisher, P.F., 2015. A critical synthesis of remotely sensed optical image change detection techniques. Remote Sens. Environ. 160, 1–14. https://doi.org/10.1016/j.rse.2015.01.006.

Tian, J., Cui, S., Reinartz, P., 2014. Building change detection based on satellite stereo imagery and digital surface models. IEEE Trans. Geosci. Remote Sens. 52, 406–417. https://doi.org/10.1109/TGRS.2013.2240692.

UN (United Nations), 2018. World Urbanization Prospects: The 2018 Revision, Department of Economic and Social Affairs. United Nations, NewYork.

Verbesselt, J., Hyndman, R., Newnham, G., Culvenor, D., 2010. Detecting trend and seasonal changes in satellite image time series. Remote Sens. Environ. 114, 106–115. https://doi.org/10.1016/j.rse.2009.08.014.

Wang, M., Hu, F., Li, J., 2011. Epipolar resampling of linear pushbroom satellite imagery by a new epipolarity model. ISPRS J. Photogramm. 66, 347–355. https://doi.org/10.1016/j.isprsjprs.2011.01.002.

Wang, J., Chen, Y., Shao, X., Zhang, Y., Cao, Y., 2012. Land-use changes and policy

dimension driving forces in China: present, trend and future. Land Use Policy 29, 737–749. https://doi.org/10.1016/j.landusepol.2011.11.010.

Wang, L., Li, C.C., Ying, Q., Cheng, X., Wang, X.Y., Li, X.Y., Hu, L.Y., Liang, L., Yu, L., Huang, H.B., Gong, P., 2012. China's urban expansion from 1990 to 2010 determined with satellite remote sensing. Chin. Sci. Bull. 57, 2802–2812. https://doi.org/10.1007/s11434-012-5235-7.

Weissgerber, F., Colin-Koeniguer, E., Nicolas, J.M., Trouvé, N., 2017. 3D monitoring of buildings using TerraSAR-X InSAR, DInSAR and PolSAR capacities. Remote Sens. 9. https://doi.org/10.3390/rs9101010.

Wen, D., Huang, X., Zhang, L., Benediktsson, J.A.J.A., 2016. A novel automatic change detection method for urban high-resolution remotely sensed imagery based on multiindex scene representation. IEEE Trans. Geosci. Remote Sens. 54, 609–625. https://doi.org/10.1109/TGRS.2015.2463075.

Woodcock, C.E., Allen, R., Anderson, M., Belward, A., Bindschadler, R., Cohen, W., Gao, F., Goward, S.N., Helder, D., Helmer, E., 2008. Free access to Landsat imagery. Science (80-.) 320, 1011.

Wulder, M.A., Loveland, T.R., Roy, D.P., Crawford, C.J., Masek, J.G., Woodcock, C.E., Allen, R.G., Anderson, M.C., Belward, A.S., Cohen, W.B., Dwyer, J., Erb, A., Gao, F., Griffiths, P., Helder, D., Hermosilla, T., Hipple, J.D., Hostert, P., Hughes, M.J., Huntington, J., Johnson, D.M., Kennedy, R., Kilic, A., Li, Z., Lymburner, L., McCorkel, J., Pahlevan, N., Scambos, T.A., Schaaf, C., Schott, J.R., Sheng, Y., Storey, J., Vermote, E., Vogelmann, J., White, J.C., Wynne, R.H., Zhu, Z., 2019. Current status of Landsat program, science, and applications. Remote Sens. Environ. 225, 127–147. https://doi.org/10.1016/j.rse.2019.02.015.

Xia, N., Wang, Y.J., Xu, H., Sun, Y.F., Yuan, Y., Cheng, L., Jiang, P.H., Li, M.C., 2016. Demarcation of prime farmland protection areas around a metropolis based on high-resolution satellite imagery. Sci. Rep. 6, 1–11. https://doi.org/10.1038/srep37634.

Xian, G., Homer, C., Fry, J., 2009. Updating the 2001 National Land Cover Database land cover classification to 2006 by using Landsat imagery change detection methods. Remote Sens. Environ. 113, 1133–1147. https://doi.org/10.1016/j.rse.2009.02.004.

Xiao, P., Zhang, X., Wang, D., Yuan, M., Feng, X., Kelly, M., 2016. Change detection of built-up land: a framework of combining pixel-based detection and object-based recognition. ISPRS J. Photogramm. Remote Sens. 119, 402–414. https://doi.org/10.1016/j.isprsjprs.2016.07.003.

Yang, C.H., Pang, Y., Soergel, U., 2017. Monitoring of building construction by 4D change detection using multi-temporal SAR images. In: ISPRS Annals of the Photogrammetry, Remote Sensing and Spatial Information Sciences. Copernicus GmbH, pp. 35–42. https://doi.org/10.5194/isprs-annals-IV-1-W1-35-2017.

Zhang, X., Xiao, P., Feng, X., Yuan, M., 2017. Separate segmentation of multi-temporal high-resolution remote sensing images for object-based change detection in urban area. Remote Sens. Environ. 201, 243–255. https://doi.org/10.1016/j.rse.2017.09.022.

Zhou, Y., Huang, X., Chen, Y., Zhong, T., Xu, G., He, J., Xu, Y., Meng, H., 2017. The effect of land use planning (2006–2020) on construction land growth in China. Cities 68, 37–47. https://doi.org/10.1016/j.cities.2017.04.014.

Zhou, Y., Li, X., Asrar, G.R., Smith, S.J., Imhoff, M., 2018. A global record of annual urban dynamics (1992–2013) from nighttime lights. Remote Sens. Environ. 219, 206–220. https://doi.org/10.1016/j.rse.2018.10.015.

Zhu, Z., 2017. Change detection using landsat time series: a review of frequencies, preprocessing, algorithms, and applications. ISPRS J. Photogramm. Remote Sens. 130, 370–384.

Zhu, Z., Woodcock, C.E., 2014. Continuous change detection and classification of land cover using all available Landsat data. Remote Sens. Environ. 144, 152–171. https://doi.org/10.1016/j.rse.2014.01.011.